# Physico-Mechanical Characterization of Kazakhstan Diatomite–Opacifier Geopolymers under Electrothermal and Conventional Curing

**Bolat Balapanov**
Department of Architecture and Construction, Institute of Engineering and Technology, Korkyt Ata Kyzylorda University, Aitekebi 29A, Kyzylorda, Kazakhstan
balapanov.sci@gmail.com

**Sarsenbek Montayev**
Industrial Technological Institute, Zhangir Khan West Kazakhstan Agrarian and Technical University, Uralsk, Kazakhstan
montaevs@mail.ru

**Orhan Canpolat**
Department of Civil Engineering, Faculty of Civil Engineering, Yildiz Technical University, Istanbul, Turkiye
canpolat@yildiz.edu.tr

**Beyza Aygun**
Istanbul Okan University, Vocational School Construction Technology Program, Turkiye
beyza.aygun@okan.edu.tr (corresponding author)

**Mucteba Uysal**
Department of Civil Engineering, Faculty of Civil Engineering, Yildiz Technical University, Istanbul, Turkiye
mucteba@yildiz.edu.tr

*Received: 11 May 2025 | Revised: 10 June 2025, 30 June 2025, and 7 July 2025 | Accepted: 9 July 2025*

*Licensed under a CC-BY 4.0 license | Copyright (c) by the authors |* *DOI: https://doi.org/10.48084/etasr.12056*

## ABSTRACT

**Focusing on sustainable construction materials, this study investigates the development of Geopolymer Composites (GCs) using Kazakhstan's abundant industrial by-products, including Fly Ash (FA), Slag (S), Diatomite (D), and Opacifier waste (OP). All precursors were sieved to below 90 µm to improve homogeneity and reactivity, and a 2:1 mass fraction binary alkali activator comprising 12M NaOH and $Na_2SiO_3$ was used at an Activator/Binder (A/B) ratio of 0.7, resulting in an Ms value of 3.29 and an estimated value for the water/binder ratio of about 0.28. Seven different GCs, ranging from single-phase mixtures containing only D and opaque to ternary combinations, were prepared and subjected to three curing regimes: ambient (23 ± 2 °C, 95% RH), thermal (80 °C for 24 h), and electrical curing (30-50V for 1-24 h). Compressive and flexural strength, capillarity, water absorption, and microstructural properties were evaluated. Electrical curing at 40 V in the 50S25FA25D series did not improve compressive strength compared with thermal curing at 80 °C; however, it improved flexural strength by approximately 13.5%, outperforming thermal curing and indicating enhanced tensile stress distribution and internal gel continuity. Although apparent porosity slightly increased by 2-3% and water absorption was 5-12% higher under electrical curing, these values remained within acceptable ranges. They were compensated by more uniform heat distribution and reduced the risk of thermal gradient cracking. The energy consumption required for electrical curing was more than 60% lower than thermal curing, making it significantly more sustainable and operationally more efficient.**

***Keywords-geopolymer; diatomite; opacifier waste; electrical curing; physico-mechanical properties***

## I. INTRODUCTION

Central Asia's material landscape is shaped not only by natural resources or extraction activities. It also reflects layers of industrial history, visible in materials such as ash, S, diatomaceous deposits, and pigment residues found across its industrial regions. Along the broad industrial belt that crosses Kazakhstan lie vast quantities of pulverized fuel ash, S, fossil diatomaceous soil, and glaze manufacturing by-products in chemically active but structurally dormant form. These materials are either stored in place or abandoned as waste, creating an environmental problem but also serving as mineralogical repositories with the potential to become generation binder systems [1-4]. The challenge is not to reproduce traditional supply chains, but to reuse and recycle waste materials. In this context, developments in alkali-activated materials—especially those optimized for locally available by-product chemistries have enabled alternative manufacturing processes, alternative to conventional cement manufacturing involving calcination and hydration-based precipitation.

Materials such as GCs, produced from low-calcium feedstocks, depend on ionic dissolution, rearrangement, and gel formation, instead of the C–S–H network, to adopt denser, chemically more resilient phases such as N–A–S–H and C–A–S–H. In doing so, they offer a thermodynamically different approach to strength development, which is not only less carbon-intensive but also considers locally available materials and environmental constraints [5-7]. This flexibility is especially valuable in Kazakhstan, where the challenge of industrial waste management and the opportunity for mineral synergism coincide with each other. FA, primarily obtained from the combustion of bituminous and lignitic coals in plants, such as those in the Ekibastuz basin, possesses high silica-to-alumina ratios combined with an amorphous glassy phase that depolymerizes effectively in an alkaline environment to produce reactive species for network development [8-11]. This FA is supplemented by S with calcium and magnesium, which induce early hardening and increased density by creating calcium-aluminosilicate hydrates. Together, these FA–S-based GCs produce binary gel systems, which can be adopted to meet mechanical performance needs and durability requirements under harsh continental climates.

Beyond these conventional materials, Kazakhstan's mineral resources also offer significant potential [11-15]. Natural D and OP, which are abundantly available but underinvestigated, can be added to modify and improve the performance of the binder. D, obtained from Miocene-era lake basins throughout Kazakhstan, consists of high internal surface area siliceous microfossils with a highly amorphous silica phase. The inclusion of D in alkali-activated mortars makes it a secondary reactive material that facilitates cross-linking gel development. It acts as a thermal and moisture buffer, postponing early drying, internal stress gradient reduction, and temperature-sensitive reaction stabilization during curing. Its pozzolanic reactivity, especially in combination with calcium-rich S, has been demonstrated to increase compressive strength by 10–20% while at the same time improving pore structure refinement.

In contrast, the role of OP involves less reactivity and more interfacial engineering. Typically, thermally stabilized oxides, such as zirconia, titania, or feldspar-based materials, comprise OP. The latter offers several structural benefits, including improved density and resistance to shrinkage [16-20]. Although OP resists dissolution in an alkaline environment, its fine particle morphology and thermal stabilization allow it to act as a microstructural filler, improving particle packing while enhancing dimensional regularity. In durability-critical systems that require resistance to cyclic environmental loading, inert fillers play an important role in limiting microcracks and improving freeze–thaw resistance, especially when combined with reactive aluminosilicate matrices.

Developing binders using new chemistry is not enough when climate and curing regimes offer their own challenges. In areas with cold climates, temperatures drop below the level required for reliable geopolymerization. At the same time, conventional thermal curing—relying on ovens, steam chambers, or sealed heaters—consumes a large amount of energy and is difficult to manage in distributed construction. The binder system must be locally available, chemically stable, energy-efficient, and have adaptive curing. In this context, electrical curing appears to be an auxiliary and integral component determining the system's overall viability. By applying controlled voltages through embedded electrodes, electrical curing generates internal heat through electrical resistance and ionic conduction, activating and maintaining the sequence of geopolymer reactions from within. This internal thermal field allows for uniform reaction kinetics and minimizes dependence on external curing equipment. Unlike external heating, in which energy is wasted to the surroundings or unequally transmitted, electrothermal techniques produce accurate thermal regimes that adjust to internal needs in the binder, assisting dissolution, gelation, and hardening without affecting dimensional integrity or energy requirements. As the demand for materials that perform structurally and address their local environment efficiently grows, electrical curing emerges as a suitable alternative.

Based on locally available materials, this study builds on standard formulations by combining various curing techniques, such as ambient, thermal, and electrothermal curing, for multiple voltages and curing periods to examine their effect on the performance of geopolymer mortars. Through application of low-voltage electrical curing (30V, 40V, 50V) over different curing periods (1-24 h), in combination with conventional thermal curing at 80 °C, this study investigates internal heat generation, reaction rates, and matrix development within such locally available materials. This experimental approach is further extended by adding in ternary mixes both chemically active (S, FA, D) and structurally passive (OP) materials. This enables complete insights into how the combined morphology-dependent curing energy influences thermal and mechanical strength and porosity behavior.

The novelty in this work lies in focusing on energy-efficient activation and comprehensive property assessment, including compression strength, bending strength, density, and absorption. These assessments are further complemented by a microstructural investigation using SEM and XRD. This

approach redesigns conventional curing in cold and low infrastructure conditions. The study also offers an efficient, scalable substitute for traditional binder materials based on Kazakhstan's mineral resources and environmental conditions.

## II. MATERIALS AND METHODS

### A. Materials

The binder components comprised ground granulated blast furnace S, Class F FA, D, and OP, all locally sourced from Kazakhstan and ground to below 90 µm to obtain homogeneous reactivity and particle size distribution. S, with a specific gravity of 2.89 g/cm³ and bulk density of 1120 kg/m³, provides dense, angular particles rich in calcium for early microstructure development. FA is spherical in morphology and has a specific gravity of 2.23 g/cm³ and a bulk density of approximately 1010 kg/m³. It contributes by supplying flowability and long-term geopolymeric reactivity via amorphous aluminosilicate components. D, with a very low specific gravity of 1.82 g/cm³ and a bulk density of about 600 kg/m³, imparts high surface area and high moisture buffering capability due to its internal porosity, enhancing capillary refinement in the matrix, while OP with intermediate characteristics, a specific gravity of 2.51 g/cm³ and a bulk density of 950 kg/m³, acts as primarily physically stabilizing filler with very little reactivity but it helps in packing behavior. The quartz sand, compliant with RILEM, has a maximum grain size of 2 mm, a fineness modulus of 2.2, and a specific gravity of 2.65 g/cm³. The quartz sand is incorporated with the binder as the inert fine aggregate to obtain uniform granulometry and a stable interface in all GCs.

The chemical compositions of all precursor materials determined by XRF are presented in Table I. The S is dominated by CaO with 51.87% and reactive silica with 28.63%, while the FA comprises predominant $SiO_2$ (43.12%), $Al_2O_3$ (18.09%), and $Fe_2O_3$ (21.68%). In comparison, D and OP contain predominantly siliceous materials, having a high $SiO_2$ content of over 79%.

### B. Mix Design

To examine the interacting effects of aluminosilicate and calcium-containing precursors in GCs, a consistent series of mortar mix was designed from different combinations of S, FA, D, and OP in various compositions. To conduct a comparative assessment of geopolymerization roles in reactivity, microstructure formation, and mechanical behavior, various combinations were used. These combinations include single-source systems such as 100S (100% of S) and 100D, the more variable combinations of 50S + 50FA, 50S + 50OP, and the more complex combinations of 50S and 25% each of the alternative binders (FA, D, or OP), as presented in Table II.

TABLE I. CHEMICAL COMPOSITION OF S, FA, OP, AND D BASED ON PRIMARY OXIDE CONTENTS

| Material | MgO (%) | $Al_2O_3$(%) | $SiO_2$ (%) | $P_2O_5$(%) | $SO_3$ (%) | Cl (%) | $K_2O$ (%) | CaO (%) | $TiO_2$ (%) | $Fe_2O_3$ (%) | MnO (%) |
|---|---|---|---|---|---|---|---|---|---|---|---|
| S | 5.29 | 7.92 | 28.63 | - | 2.30 | - | 1.16 | 51.87 | 1.16 | 0.44 | 0.60 |
| FA | 2.03 | 18.10 | 43.12 | 0.84 | 0.42 | 5.01 | 0.60 | 4.95 | 2.14 | 21.68 | 0.35 |
| OP | 0.55 | 4.26 | 82.89 | 0.44 | - | - | 2.62 | 1.34 | 0.76 | 6.77 | - |
| D | 0.72 | 5.43 | 79.70 | 0.41 | - | 2.11 | 2.18 | 1.13 | 1.03 | 6.72 | - |

TABLE II. MIX PROPORTIONS OF GCs (kg/m³)

| Mixture | OP (kg/m³) | D (kg/m³) | FA (kg/m³) | S (kg/m³) | $Na_2SiO_3$ (kg/m³) | NaOH (kg/m³) | Sand (kg/m³) |
|---|---|---|---|---|---|---|---|
| 50D25FA25S (0.7) | 0 | 200 | 100 | 100 | 186.67 | 93.33 | 1000 |

All constituents were weighed and mixed with standardized RILEM sand (0–2 mm, a specific gravity of 2.65 g/cm³, and a fineness modulus of approximately 2.2) in a binder to aggregate ratio of 1 to 2.5 to preserve granulometric homogeneity. Alkali activation was provided by a 12M NaOH and $Na_2SiO_3$ solution in a 1 to 2 mass ratio, equivalent to an Ms of 3.29. This solution was added at an A/B ratio of 0.7, accounting for an estimated water to binder ratio of 0.28, including bound water within the chemically reactive silicate phase. Preparations of activator solutions were made at least 24 h before the day of the mixture to stabilize temperature and viscosity. The mixing was initiated with 2 min of dry mixing of the binders and the sand, followed by a 3-min wet mixing. The activator was added until a homogeneous and workable mortar mixture was achieved. After homogenization, fresh geopolymer mortar was cast into prismatic molds, strictly complying with TS EN 196-1 protocols and laboratory best practice in order to ensure reproducibility and accurate dimensions.

For electrothermal curing groups, two high-purity copper electrodes were attached symmetrically along opposite internal vertical faces of the mold with an imposed inter-electrode separation. These were seated flush within internal walls and mechanically secured for stable positioning throughout casting. Electrode ends projected from the mold body, allowing external attachment to an adjustable sinusoidal AC power unit (variable output voltage). Casting was conducted in two equal steps: pouring and compacting half of the mortar using a calibrated vibrating table for 30 s, ensuring uniform distribution of particles by entrapped air removal. A second layer was added, followed by a 45–60 s compaction, ensuring full matrix consolidation. The top surface was manually leveled using a stainless-steel trowel immediately after casting, ensuring surface regularity and dimensional consistency while avoiding excessive pressure that could interfere with internal matrix structuring. Following leveling, the molds were sealed with a thick, vapor-permeable plastic membrane to conserve internal moisture and avoid premature drying or ambient carbonation within the fresh mortar, especially at early stages of initial setting and early geopolymerization. Sealed samples were then subjected to one of three well-controlled curing regimens to separate the physicochemical effects of different activation environments.

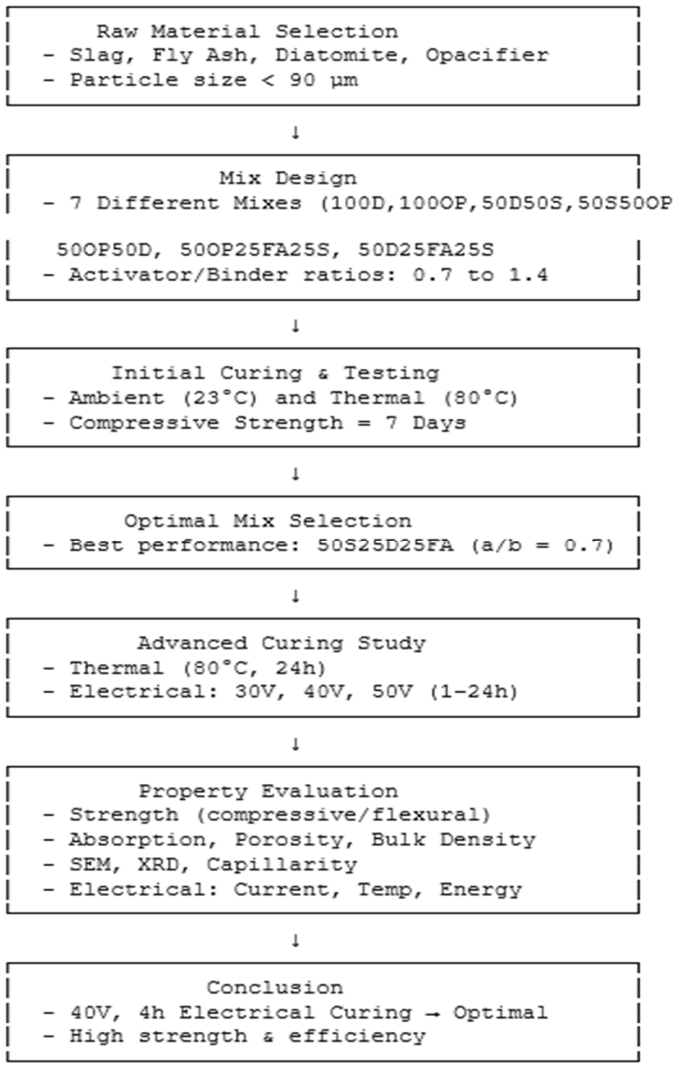


Fig. 1. Flowchart of the experimental program.

The ambient curing involved placing covered molds within a humidity-saturated chamber at constant 23 ± 2 °C, ≥95% RH for 24 h. Following the initial 24 h, samples were demolded and transferred into a room-temperature-controlled laboratory (23 ± 2 °C, 50% RH) environment for continued hydration until the test periods. In contrast, for thermal curing, covered samples were similarly kept undisturbed for 24 h, then demolded and transferred into a pre-heat-treated laboratory convection oven maintained at 80 ± 1 °C. Upon curing, the oven was turned off, leaving specimens to cool passively for a minimum period of 3 h to avoid thermal shock before they were stored under ambient conditions. In electrothermal curing, immediately after casting, copper-electrode-embedded specimens were attached to a sinusoidal alternating current (AC) power unit with constant voltages of 30V, 40V, or 50V, depending on the experimental group. AC generates volumetric heating through Joule dissipation ($Q = I^2R$), with distributed resistive heat generation supported by the ionic conductivity of fresh geopolymer matrix. In contrast to DC systems, AC operating at 50 Hz is free from any electrode polarization, directional ion migration, and localized electrochemical degradation, ensuring uniform electrochemical balance and heat. Internal temperatures were monitored continuously using centrally embedded K-type thermocouples with peak core temperatures between 70 and 85 °C, depending on voltage level and time. Simultaneously, current flow tapered off as ionic mobility was reduced due to gelation, reflecting progressive polymerization and establishing a natural feedback heat loop. Specimens, after voltage removal, were passively cooled in the mold to ambient temperature before demolding, achieving gradual thermal equalization with reduced potential for internal microcracking.

### *C. Methods*

Physical and mechanical testing were performed on 40 × 40 × 160 mm prismatic specimens, with three identical samples ($n$ = 3), prepared and tested for each mixture and curing condition to ensure repeatability and statistical confidence. These standardized samples were used to assess the influence of various curing regimes over time. The ASTM C642 standard was used to measure water absorption, apparent porosity, and bulk density by measuring oven-dried, saturated-surface-dry, and immersed specimen masses, facilitating accurate matrix compactness and pore volume determination. Capillary absorption was measured in accordance with ASTM C1585. For capillary absorption, the lateral surfaces of dried prisms were coated with epoxy, and the bottom surfaces were subjected to 3 ± 1 mm of deionized water; mass increments were recorded at 1-min to 24-h intervals, followed by the calculation of the sorptivity index (I-value). The I-value is determined by normalizing cumulative sorption by the square root of time to accommodate adherence to one-dimensional flow requirements.

The flexural strength was determined in accordance with ASTM C348, using a three-point flexural setup on a 100 mm span, and a loading rate of 50 ± 10 N/s. The compressive strength was tested on fractured halves in a uniaxial loading machine with a loading rate of 2.4 ± 0.2 kN/s. The compressive strength test was conducted in accordance with ASTM C349. Physical and mechanical tests were routinely conducted following 7 and 28 days of curing to represent early age development and more extended hydration across different activation regimes. Microstructural characteristics were also examined by SEM in accordance with ISO 16700:2007, where gold-sputtered fracture surfaces from core areas were investigated using 15–20 kV accelerating voltage to observe gel morphology, residual phases from precursors, and interconnecting pores. Simultaneously, phase identification and crystalline development were assessed employing XRD in accordance with ASTM C1365, using a Cu-Kα radiation of λ = 1.5406 Å, a 5°–70° 2θ scanning range, and a 0.017° step size to identify the impacts of precursor chemistry and curing styles on the geopolymeric matrix.

## III. RESULTS AND DISCUSSION

### *A. Mechanical Properties*

The compressive strength results, shown in Figure 2, refer only to an initial short-term assessment period, within which every geopolymer mixture—comprising various S, FA, D, and OP combinations—was tested under ambient and heat curing

conditions for only 7 days. This specific 7-day test was intended as a selection mechanism, facilitating the identification of optimum mix configurations and A/B ratios on the basis of early-age performance. For this, every mixture was subjected to one or more A/B ratios (e.g., 0.7, 0.9, 1.1, 1.4), depending on precursor-specific factors. The most promising mix combinations, identified using this preliminary screening, were then advanced to the main experiment, where longer curing times (7 and 28 days) and detailed physico-mechanical and microstructural analyses were conducted under all three curing conditions.

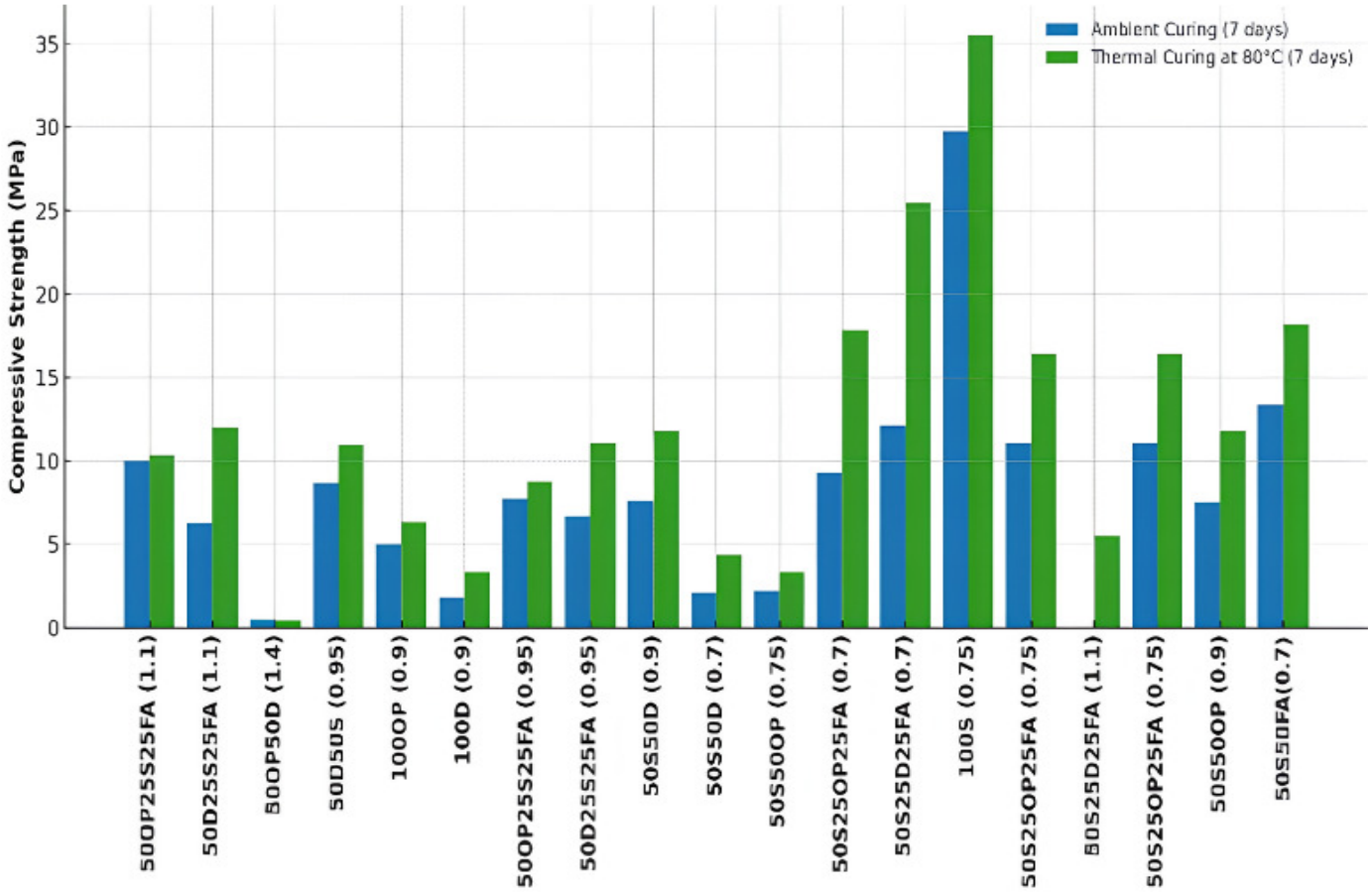


Fig. 2. Effect of ambient and thermal curing on the compressive strength of related binary or ternary GCs with varying A/B ratios.

Figure 2 illustrates consistently higher early-age strength under thermal curing (80 °C, 24 h) compared to ambient curing (23 ± 2 °C, ~95% RH). This higher early-age strength can be attributed to increased reaction kinetics. In the case of geopolymerization, heat enhances the dissolution of the silicate and aluminate species from reactive materials, such as FA and S, resulting in rapid polycondensation and dense gel formation. The most significant effect of heat is seen in the 50S25D25FA (0.7) mixture, where the average compressive strength increased from 13.39 MPa under ambient curing to 30.63 MPa under thermal curing, representing a 129% increase. Such a significant improvement indicates a synergistic interaction among the calcium-bearing S, the pozzolanic FA, and the fine amorphous D acting as a source of supplementary silicate and a microfiller that increases the packing density and decreases porosity.

Additionally, D is also well-known for having a very high surface area and porosity, which significantly enhances the amount of reactive surface area available within geopolymer matrices. Such features have been observed to improve the dissolution of siliceous phases and improve gel formation during heat curing, as evidenced by earlier reported BET surface area measurements ranging from approximately 40 to 80 m²/g, much larger than those of traditional precursors like S or FA.

The 50S25OP25FA (0.7) followed a similar trend, from 11.08 MPa under the ambient curing to 20 MPa (average) under thermal curing, representing an 80.5% increase. This improvement can be attributed to the catalytic role of heat when both FA and S are combined. The 50S25D25OP (0.9) had a comparatively low compressive strength of 8.52 MPa under ambient curing and 12.73 MPa under heat activation. The poor performance of 50S25D25OP (0.9) can be attributed to the intrinsically low chemical reactivity of the D and OP phases, exacerbated by the lack of FA, which is an essential source of amorphous aluminosilicates for geopolymerization. In the absence of high-reactivity FA, the released silicate and aluminate species from the reactants are significantly restricted,

leading to limited expansion of the gel phase and a poorly bonded, porous structure [20-23]. As a result, D and OP can play only a minor role in physical mechanisms such as microfilling and heat buffering. Still, their low reactivity—especially under ambient and moderately high temperatures—indicates the progress of a dense, fully connected aluminosilicate network. As a result, GC's capacity to react spontaneously to heat curing is curtailed, leading only to a moderate 49% strength increase [17-20].

On the other hand, the 50S50FA (0.7) binary system yielded an average compressive strength of 13.39 MPa under ambient curing and 18.65 MPa under thermal curing. This indicates that the combination of S and FA has a more dispersed, less temperature-dependent reaction kinetics compared to the case of a three-component system containing additional siliceous fillers, such as D or OP, even though their chemical compositions are compatible. The absence of the third component limits the complexity of the resulting gel structures, and at the same time, facilitates the stability of reactivity and homogeneity. The difference in the performance of these two systems highlights the role of the synergy of the precursors and the balance of composition in attaining high early-age strength, as well as sensitivity to heat acceleration in the GCs.

In contrast, 100D (0.9) and 100OP (0.9) did not exceed 6.5 MPa even under thermal curing, showing their poor performance as single binders. In particular, the strength of 100D (0.9) improved only from 1.80 MPa, under ambient curing, to 3.36 MPa, under thermal curing, suggesting that despite the silica richness of D enhancing modest geopolymeric activity with heat, the lack of proper content of alumina—and more importantly, of calcium—may have prevented the formation of more cohesive or cross-linked gel networks in this specific system. It is recognized, nonetheless, that a strong gel can be formed in other low-calcium systems as long as there is proper balancing of reactive silica and alumina content.

Similarly, 50OP50D (1.4) with strengths consistently around 0.45 MPa irrespective of the curing techniques demonstrated that excessive dilution of active-binder phases by inert fillers limits any appreciable strength gain, perhaps because of agglomeration or poor dispersal of activator ions. 50D50S (0.95) displayed comparatively moderate improvements: from 8.67 MPa (ambient curing average) to 10.93 MPa (thermal curing average), an increase of 26%, indicating that even as the S contributes reactivity, the lack of FA limits the gel-forming efficiency under heat. Even in the case of the third-component-containing ternary systems, the type of third component matters significantly. The 50S25D25FA (0.7) had a higher compressive strength compared to 50S25OP25FA (0.7) and 50S25D25OP (0.9), indicating that the reactivity of FA under heat treatment is greater than that of both OP and D, and that, in combination with them in optimal proportions, promotes a co-gelation process that better fills up pores, increases the homogeneity of the matrix, and contributes to increasing tensile strength as well as resistance to cracks. The effect is highlighted by the moderate performance of 50S50D (0.9) that attained a compressive strength of only 7.56 MPa under ambient curing and 11.76 MPa under thermal curing, reinforcing the point once more that, in the absence of FA, even balanced blends with D and S are insufficient in early strength gain.

Furthermore, the compressive srength of 50S25OP25FA (0.75) increased from 11.10 MPa to 16.44 MPa, indicating that even at the ever-so-slightly modified A/B ratio, the FA and OP combination is even active under heat but weaker in action compared to the FA and D. A/B ratios of 0.7 have been consistently more effective, as evidenced in nearly all the top-performing mixes. In that regard, 50S25D25FA (0.7) emerges as the best formulation due to its peak compressive strengths and consistent and repeatable performance under ambient and thermally accelerated curing regimes. The capacity of the mixture to achieve high early strengths, while using only industrial by-products, also has its potential in sustainable construction. Moreover, its rational response to electrical charging with low voltage or moderate heat, without delay, makes the mixture particularly suitable for cold climate regions where normal ambient curing is ineffective.

The compressive–flexural strengths of the 50S25D25FA and 50S25OP25FA series with thermal curing exhibit significant improvements through ternary systems. 50S25OP25FA, under ambient curing, has a median compressive strength of 9.33 MPa, which increased to 17.80 MPa through thermal activation, representing an improved increment of 91%. In comparison, the OP-based system, based on predominantly inert-characteristics, containing ceramic waste, offers minimal early-stage reactivity. Particles within its matrix—glassy, sintered, crystalline—have insufficient amorphous silica or alumina to meaningfully contribute toward gel formation, thereby functioning as fillers that limit rather than enhance gel interconnectivity.

The strength difference becomes apparent after thermal curing at 80 °C for 7 days. The 50S25D25FA develops an average compressive strength of 25.39 MPa, whereas the 50S25OP25FA series achieves only 17.84 MPa, a significant difference of 42.3% compared to 50S25D25FA. This difference is measured by the Thermal Activation Coefficient (TAC), defined as the ratio of the 7-day compressive strength under thermal curing to that under ambient curing. TAC is 2.099 for the D-based mix and 1.912 for the OP-based mix, reflecting a 9.8% greater thermal reactivity of the D25 series. The higher ionic mobility under heat and the higher reactivity of the D-based phases are responsible for the better activation. Higher specific surface area of D and its higher content of amorphous silica allow for supplementary gel nucleation, whereas its porosities help reduce internal heat devitrifications by spiking natural conduction within it. They also hinder the microcracking of its surface during exothermic curing.

The OP system continues only with incremental advances, due to its lower reactivity phase content and thermal insulating ability, as it restricts uniform thermal conduction and deep gel infiltration. Again, the evidence of long-term activity of $Mg^{2+}$ ions, along with sustained densification processes within the D-based framework, is established by continued dominance by the D-based mix after 28 days under identical thermal environments. In the compressive strength test, the 50S25D25FA mix achieved a strength of 31.72 MPa compared to 19.80 MPa for the OP-based series, equivalent to a 60.2%

difference in structural efficiency. The Long-Term Thermal Activation Coefficient (LTAC) value, as determined by the ratio of 28-day thermal-to-ambient strength, is 2.622 for the D-based mix compared with 2.122 for the OP blend—a 23.6% relative improvement in long-term efficiency of heat utilization. This further confirms the continued activity of $Mg^{2+}$ ions, along with ongoing processes of matrix densification within the D-based matrix. Further, the Strength Retention Ratio (SRR), as determined by the ratio of 28-day-to-7-day strength, is 1.25 for D25 compared with 1.11 for OP25. This higher, 14% long-term gain indicates an extended lifespan of reactive consolidation, as the D-based matrix makes the best of deep diffusion, followed by gradual crystallization of the strengthening phases. In contrast, the OP-based matrix reaches mechanical plateau prematurely, as a consequence of filler saturation as well as poorer gel continuity. These trends are also reflected in the flexural strength values, further confirming the benefit of the D-based matrix. Under ambient curing, the flexural strength for 50S25D25FA was 3.82 MPa, a 21.3% improvement over the OP equivalent's estimated 3.15 MPa. Following 28 days of thermal curing at 80 °C, the flexural strength was 6.06 MPa for D25 compared with 4.01 MPa for OP25, representing a 51.1% improvement in tensile strength.

Flexural Strength Thermal Enhancement Ratio (FSTER) is defined as the ratio of 28-day flexural strength to the flexural strength under ambient curing. For the D-based system, FSTER was 1.59, compared to 1.27 for the OP system, reflecting a 25.2% greater flexural strength gain. These gains can be directly attributed to developing well-ordered, highly interconnected polymeric gel networks within the D-based matrix, permitting optimal stress transfer and bridging of cracks. Additionally, ductility is further elevated, as well as reducing stress concentration zones, by the presence of Mg-containing phases within the D25 system compared with the OP system, where the discontinuities created by inert particles detract from resistance to crack propagation. Another measure of interactiveness is the Compressive-Flexural Synergy Factor (CFSF), defined as the product of the compressive and flexural strengths after 28 days. The CFSF of 50S25D25FA was $31.72 \times 6.06 = 192.3$ $MPa^2$, whereas for the OP-based mix it was $19.80 \times 4.01 = 79.4$ $MPa^2$, indicating a 2.42 times greater combined mechanical efficiency for the D-based mix. This parameter is very useful to assess suitability for structural applications, where multiaxial stress conditions prevail, and both compressive and tensile integrity are required.

Combined strength demonstrated by the D-based series suggests a matrix that is resistant to compressive and tensile failure over its service lifespan. This can be attributed to higher internal coherence, with $Mg^{2+}$ aiding the development of hydrotalcite-like phases that strengthen the matrix by bridging microvoids and reinforcing weak areas. These gels aid in tighter packing, lowering pore interconnectivity, and a harder transition region between the aggregate and binder. Magnesium presence further aids early gel network development by breaking the energy barrier for bond formation between silicates, promoting higher interconnectedness and stability of the framework. D contributes to this by providing reactive silica and finely dispersed sites for nucleation, accelerating matrix compaction. In contrast, the composition based on perlite is less integrated, as gel continuity is disrupted due to the passive nature of its fillers, promoting anisotropic stress response. The consequence is a higher tendency for microstructure fracturing and a lower load distribution capacity, especially under tensile load or cyclic thermal exposure [16-19]. The results of various compressive and flexural tests are illustrated in Figure 3.

The outstanding mechanical and microstructural performance of the 50S25D25FA is best explained by its excellent electrothermal curing behavior, most notably under sustained 40V application, as reflected by its record compressive strength of 30.63 MPa as well as by a very high-efficiency energy-to-strength conversion ratio. Under such a condition, the mixture reported a maximum current of 0.67 A at 1 h, combined with an abrupt internal temperature rise from 28 °C to 76 °C, with core temperatures increasing to as high as 90 °C, as a result of Joule heating spread volumetrically through the conductive paste. The average current over the active 5-h curing regime was constant at 0.302 A, leading to an overall 60.33 Wh (217,200 J) total energy input and a corresponding average nominal power draw of 12.07 W. An average resistance of about 132.45 Ω is computed from Ohm's law using the average voltage. An estimated 0.76 S/m of resulting electrical effectiveness using an assumed 2 cm electrode gap and 10 $cm^2$ surface area, then falling gradually to a value under 0.01 S/m as gelation proceeds and ionic paths become hindered by the polymerization of the solid phase. This change, as seen in the current-time decay curve—decreasing from 0.67 A to 0.27 A by 3 h, then onwards to 0 A by 24 h—reverses the sequence of the thermo-chemical stages of geopolymerization: dissolution of aluminosilicates, nucleation of the oligomeric species, network gelation, and hardening of the microstructure. As portrayed in Figure 4, the current decay under 40V curing conditions is a non-linear but an exponential function, typical of a reaction-limited system in which the cumulative depletion of mobile ionic species is associated with an increase in electrical resistivity controlling the conversion rate. The initial exponential decrease is a sign of the continued process of geopolymerization, where the matrix gradually evolves from a conductive, ion-rich to a consolidated, electrically insulating solid by the formation of a connected aluminosilicate gel network. The current response under 30V is a very gradual approach to a low peak of 0.50 A, associated with a limited thermal output that does not exceed 63 °C. The energy input of 38.38 Wh under 30V curing conditions was sufficient to maintain electrical conductivity for an extended period, as suggested by current levels above 0.12 for up to 5 h. Still, it ultimately proved insufficient to achieve full gel densification. This partial energy dissipation likely led to incomplete geopolymer network formation, resulting in high capillary porosity, delayed setting kinetics, and an underdeveloped microstructural framework. As a result, the matrix exhibited reduced mechanical performance, with significantly lower compressive strengths observed in the relevant trials, reflecting insufficient thermal and ionic stimulation required to achieve a fully polymerized and structurally coherent binder phase.

At 50V, while temperature climbed to 93 °C in the first hour, the current dropped to 0.01 A by the fourth hour,

signifying localized overcuring accompanied by electrical insulation of the surface layers as the interior most probably remained undercured. Such non-uniform thermal profiles conform to the thermographic trend of geopolymer materials that possess low thermal conductivity values (approximately 0.6–0.9 W/m·K). These conditions induce differential vapor pressure, microcracking, and interface delamination, particularly in the case of acceptable, porous additives such as D. Even at high thermal power potential, 50V had a power draw of only 25.83 Wh because of premature current withholding, demonstrating that the maximum voltage is not proportional to the optimal energy efficiency or mechanical performance. These same plotted curves of temperature and current, interpreted in combination, further demonstrate the synchronized coupling of chemical kinetics and thermal input. At 40V, the corresponding temperature and current peaks in the first hour, followed by a simultaneous drop in both over the next three hours, illustrate that the system functions in a controlled thermokinetic window, allowing for complete formation of the geopolymer network. In the case of the D component, its high amorphous silica and internal porosity, which, in addition to increasing the exposed surface area available for reaction, provides a pseudo-capacitive effect by holding ionic species and prolonging conductivity, as well as postponing the onset of dangerous thermal runaway. The 40V energy input—expressed as approximately 60 Wh per 1000 cm³ of paste—also compares/is also compared favorably to the established thermal capacity of such a system (approximately 1.6 kJ/kg·K). From the specific heat equation ($Q = m \cdot c \cdot \Delta T$) and an estimated 1.8 kg mass for the volume under test, a 50 °C rise demands approximately 144 kJ, consistent with the measured input of 217 kJ, validating electrical to heat conversion without the existence of any external loss. Such an energy-material fit achieves the maximum internal heat utilization. It controls the dangers of overcuring due to temperature surges over 100 °C, in which the resulting vapor pressure can lead to internal voids or cracking.

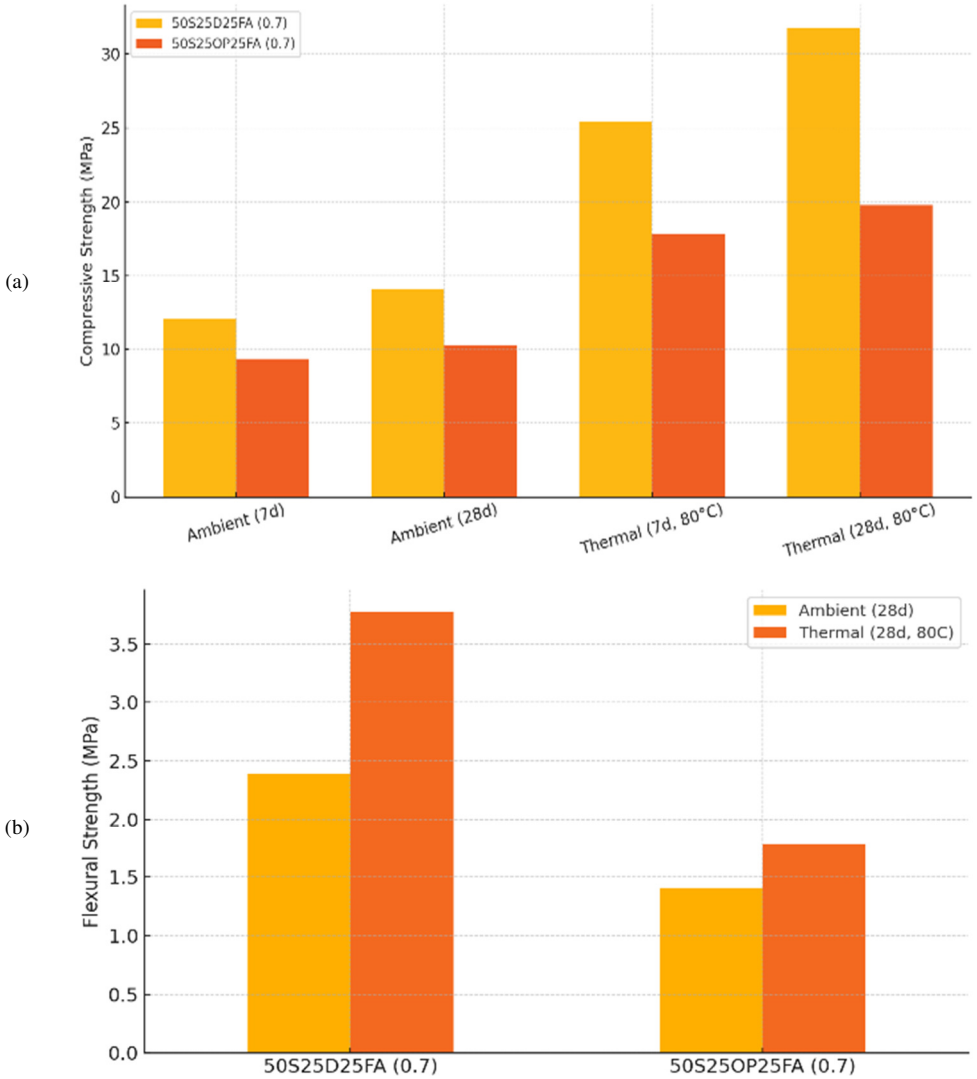


Fig. 3. Strength of 50S25D25FA and 50S25OP25FA mixtures under ambient and thermal curing conditions: (a) compressive strength, (b) flexural strength.

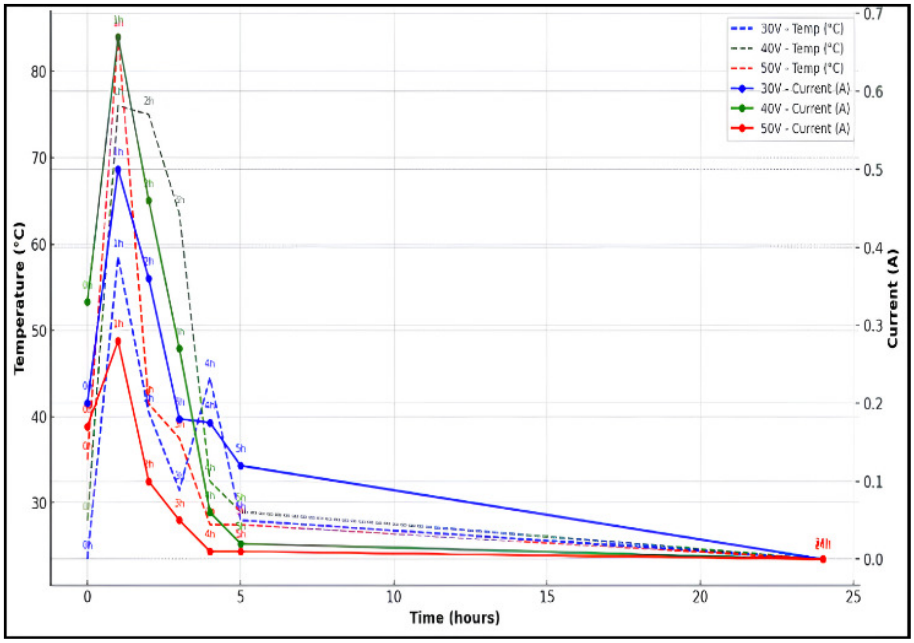


Fig. 4. Temperature and current evolution during electrical curing of GCs under 30V, 40V, and 50V regimes over 24 h.

Electrically, the system evolves from an originally low-resistance ionic conductor to a high-resistance dielectric, with decreasing permittivity as mobile ions are absorbed and immobilized within aluminosilicate chains. This change is accompanied by a significant reduction in carrier concentration with a corresponding rise in resistivity, so that the current flow indicates a reliable in-situ monitor of reaction advancement. In contrast to thermal curing, in which external sensors can only measure near-surface temperature, electrical curing combines reaction kinetics and internal heat generation, removing temperature gradients, and thus matrix inhomogeneity. From the perspective of a construction engineer, such behavior makes the 50S25D25FA composition under 40V curing an excellent candidate for cold-weather construction, precast manufacturing, and high-energy-saving concrete alternatives, where conventional thermal curing is impractical or expensive. The optimum 0.7 activator-to-binder ratio maintains an appropriate alkalinity level to induce dissolution reactions without promoting free water content, potentially causing porosity and shrinkage. Electrical efficiency, temperature control, and completeness of responses yield a 129% compressive strength increment compared to ambient curing and an extremely dense microstructure backed by interpenetrating gel phases. Finally, the electrothermal behavior of 50S25D25FA under 40V curing is a balanced synergy of voltage-stimulated heat, time-governed ionic conductivity, and phase-specific chemical reactivity, an excellent system for emerging electrically-cured-GC [24-26]. Figure 5 presents a comparison of compressive strengths of GCs under 30V, 40V, and 50V electrical curing for 1–24 h.

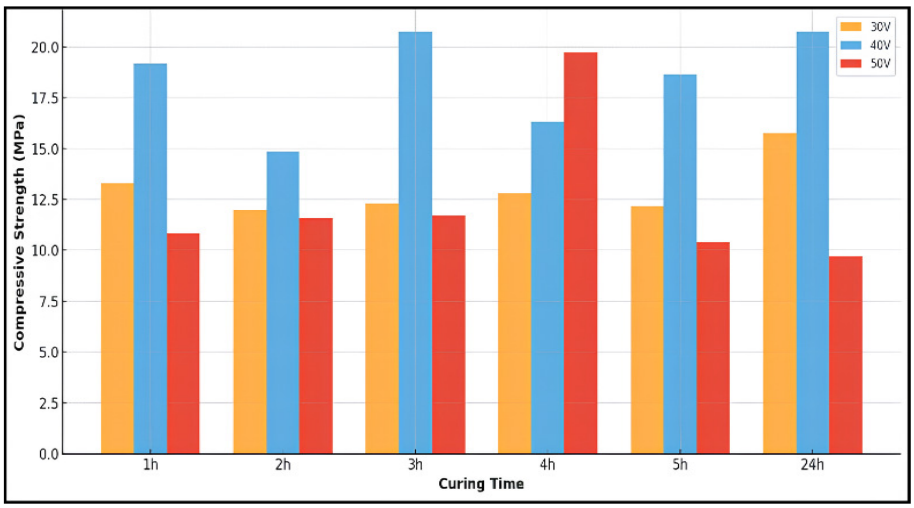


Fig. 5. Comparison of compressive strengths of GCs under 30V, 40V, and 50V electrical curing for 1–24 h.

The compressive strength of the 50S25D25FA at various electrical curing voltages—30V, 40V, and 50V—shows the direct effect of heat energy on the process of geopolymerization. It also highlights the critical interrelation among several electrochemical, material-dependent, and microstructural factors influencing the effectiveness of early-age binder refinement, as depicted in Figure 5. Among the curing regimes investigated, the 40V curing condition demonstrated the maximum effectiveness, with the mixture building the ultimate compressive strength of 20.76 MPa at 3 h, yielding 20.75 MPa at 24 h, and registering a total 8.3% early-age strength stabilization in the first few hours. This indicates a strong and consistent reaction pattern, in which the internal heat, precursor synergy, and reaction kinetics existed in equilibrium. Significant difference in early strength development was noted, with the 40V curing condition yielding compressive strengths about 49% higher than those for 30V and a 114% higher than the ultimate strength developed after 50V. This highlights 40V as the best voltage for triggering and maintaining uniform microstructure development within the first 24 h. In comparison, the 30V condition, though indicating gradual improvement from 13.3 MPa up to 15.76 MPa—a gain of 18.5%—was characterized by a slow initial response, reflective of subcritical activation energy and insufficient thermally stimulated activation, thus limiting early gel nucleation as well as matrix compaction. Unfavorable internal temperatures most probably inhibited the leaching of the less reactive phase, i.e., FA and D, leading to a less compact gel structure and higher porosity. The densification coefficient of this system, defined as the ratio of the 24-h strength (15.76 MPa) to the 1-h strength (13.3 MPa), was 1.18, whereas that of the 40V system, as noted earlier, was 1.08. This indicates that the 40V system developed most of its strength early and attained a saturated phase. I contrast 30V, gained its strength late in the curing process.

The 50V curing regime demonstrated unstable strength development. After an initial low value of 10.84 MPa at 1 h, the mixture rapidly increased the strength to 19.74 MPa at 4 h, followed by a sharp decline to 9.7 MPa at 24 h, representing a 50.8% loss from the peak strength and a 10.5% decrease relative to its initial value. This irregular trend suggests structural degradation and internal failure mechanisms such as microcracking, interfacial debonding, or moisture loss due to excessive and uneven heating. The degradation coefficient—the ratio of 24-h strength to peak strength—was 0.49 in the 50V system, indicating that nearly half the strength gained was lost within the first 20 h of curing. In contrast, the same ratio for the 40V system was 0.99, reflecting near-total retention of mechanical integrity. From a material perspective, the high performance under 40V can be attributed to harmonizing reactivity among precursors and optimum energy transfer into the system. S, 50% of the binder system, is an effective early-stage activator, providing readily available $Ca^{2+}$ that induces the rapid nucleation and progress of C–A–S–H gels that form the early structure of mechanical strength. Simultaneously, FA and D serve as a vital source of reactive alumina and silica, which allow for the sequential formation of N–A–S–H gels that reinforce the microstructure, improve durability, and achieve long-term stability using prolonged polymeric cross-linking. The key controlling factor is the heat accessibility: under 40V, internal matrix temperatures range from within the critical 70–80 °C range for at least 2–3 h, providing sufficient time for aluminosilicate source dissolution, polycondensation, and cross-linking of the network. This facilitates the early establishment of a rigid structure and chemical-bonded framework.

Reactivity Realization Index (RRI) was calculated by comparing the actual compressive strength at 3 h to the maximum theoretical potential based on precursor reactivity. For the 40V case, assuming the system's reactant potential to achieve up to 22 MPa, the RRI at 3 h equals 20.76/22 ≈ 0.944, compared to 12.3/22 ≈ 0.56 under 30V curing and 11.69/22 ≈ 0.53 under 50V curing at 3 h, showing that 40V achieves almost full reactivity utilization early. Another parameter, the Structural Retention Index (SRI), can be defined as the ratio of the 24-h strength to the 3-h strength. In the case of 40V, it equals 20.75/20.76 ≈ 1.00, indicating very high structural stability, whereas for 50V, 9.7/19.74 ≈ 0.49, indicating extreme degradation over time. This difference in SRI highlights the danger of crossing the optimal temperature window. Since 50V induces excessively rapid reactions ahead of water retention and internal gel reorganization, leading to both physical shrinkage and chemical discontinuity. Ultimately, by comparing the efficiency in terms of strength per unit of supplied energy, the 40V curing condition again outperformed the others. A total energy input of 60.33 Wh produced 20.75 MPa, with an efficiency of 0.344 MPa/Wh, compared to 0.411 MPa/Wh at 30V (due to the low energy input of 38.38 Wh) but with considerably reduced total strength. Under 50V curing, the value drops to 0.375 MPa/Wh due to premature energy cut-off and poor retention. Although the 30V curing can be more 'efficient' in a numerical sense, the absolute performance is still insufficient to be useful in structural performance. The 40V, therefore, not only provides optimum structural performance, but also has efficient energy utilization, minimizes degradation, and maximizes GC activation.

The flexural strength of the 50S25D25FA under electrical curing regimes of 30V, 40V, and 50V is governed by a combination of thermal gradient diffusion, dissociation efficiency of ions, matrix elasticity, and early-stage gel continuity, all of which contribute in the tensile integrity of the hardened matrix. Under the 40V curing regime, which yielded the most mechanically sound result, the flexural strength increased to 6.88 MPa at 24-h, with a Cumulative Strength Evolution Rate (CSER) of about 0.28 MPa/h throughout the curing duration. Its smooth progression indicates an internally uniform geopolymer matrix, in which polymerization fronts propagated continuously. The S, FA, and D reactant aluminosilicate species were optimally incorporated into an intervening, dense, and connected gel network.

The Structure Consistency Factor (SCF), defined as the ratio of variation in hourly strengths to the 24-h maximum strength, was only 0.086 for 40V, indicating negligible internal degradation or phase separation over the curing period. The system demonstrated high tensile transfer consistency in the axial direction, as it consistently retained 92%-100% of its 3-h flexural peak strength during the subsequent curing period.

Such behavior reflects that the silicate gel chains had attained a high enough connectivity and maturity to efficiently withstand tensile stresses, resisting elastic deformation and shear-induced displacement. This represents a well-organized, load-carrying polymer network with high dimensional stability under flexural strain. In contrast, under 30V curing, although the mixture demonstrated very encouraging flexural behavior (6.65 MPa at 1-h), the performance did not last longer, declining to 5.43 MPa at 24-h, a net loss of approximately 18.3%, corresponding to a Flexural Decay Velocity (FDV) of –0.051 MPa/h after the peak. Such a decline in flexural strength indicates the existence of unfulfilled pore networks and inadequate microstructural stitching—conditions that lead to early hardening but result in delayed redistribution of stresses under bending loads.

The Effective Gel Continuity Coefficient (EGCC), defined as the ratio of the 3-h to 24-h flexural strength, was 0.79, far less than the unity value expected from a fully matured geopolymer matrix. The lower value of EGCC indicates that while the system attained early mechanical hardening due to S-based C–A–S–H, the time-temperature exposure was insufficient to fully engage the FA and D phases, especially in the planar directions, subjected to bending stress. In 50V, the thermal environment created by the high voltage resulted in internal peak temperatures over 90 °C, but the flexural strength declined sharply. After reaching a maximum of 5.88 MPa during the initial hours, the strength declined to 3.74 MPa at 24 h, representing a cumulative degradation of 36.4%. This correlated with a Coefficient of Thermal Overstress (TOC), a measure of the loss in strength per unit increment more than the optimum reaction range (assumed to be approximately 80 °C), of –0.144 MPa/°C, suggesting supercritical temperature sensitivity. Rapid surface layer solidification and a lack of proper energy transfer to the core (caused by sudden current removal) most likely resulted in shear planes and microscopic delamination zones, significantly reducing tensile strength. These observations are confirmed by the Flexural Ductility Gradient (FDG), defined as the difference between the mid-point (3-h) and end-point (24-h) flexural strength gradients, with a value of -2.21 MPa for the 50V curing condition compared to +0.47 MPa for the 40V curing condition. A negative FDG of -2.21 indicates the localization of stresses, likely by vaporization-induced shrinkage or thermally activated crack formation in the matrix.

Electrically, the GC acts as a self-controlling system of dynamics, with its tensile resistance capacity intrinsically tied to its potential for localized redistribution and migration of the charge in the early phases of gel network refinement. GC under 40V demonstrated a balanced development of electrical resistivity, gradually changing from a very conductive ionic environment to a stabilized dielectric state—a necessary change for silicate chains to be oriented in the most flexurally loading-susceptible planes. Controlled electrical activity allowed good energy distribution throughout the matrix and uniform gel chain orientation, especially in tensile performance-critical directions. The Anisotropic Stress Propagation Coefficient (ASPC), defined as the correspondence of peak flexural strength to the directional resistive energy stream from the electrodes, was the highest under 40V curing, indicating better lateral gel connectivity and matrix densification. In contrast, 30V had a low Ionic Reaction Uniformity Index (IRUI) due to its poor current mobility and sub-threshold heating, which restricted adequate Si–O–Al cross-linking in regions of potential stresses.

In 50V, the premature current loss and the development of high-temperature barriers in the vicinity of electrodes compromised the Electromechanical Coupling Ratio (EMCR), indicating the ineffectiveness of the energy transfer to the flexural-critical regions. Material-wise, D's flexural strengthening is based primarily on activation temperature and interaction time. At 40V, D's high-surface-area siliceous particles could dissolve step by step and engage in lateral gel expansion, adding toughness and cracking resistance. At 30V, its activation remained restricted, forcing it to act as a filler only. At 50V, its porous structure can potentially allow water loss and the formation of vapor escape zones, disrupting structural continuity. In addition, early rigidity came from the S, and FA added flexural resiliency through spherical particle packing and long-chain polymer network refinement—both of them fully developed only under the controlled heat and conductivity environment provided by 40V [21, 27, 28]. Figure 6 illustrates a comparison of the flexural strengths of GCs under 30V, 40V, and 50V electrical curing for 1-24 h.

### *B. Physical Properties*

The results of 50S25D25FA, subjected to various curing conditions (ambient, thermal, and electrical curing by 30V, 40V, and 50V), water absorption analysis, apparent porosity test, and bulk density analysis indicate interdependence of the thermal-electrical input, gel development, and resulting quality of the micromatrix. The trends derived from these experiments correlate well with the mechanical strength characteristics and provide insights into matrix maturity, phase stability, and permeability, all of which are critical for long-term durability. In case of ambient curing, water absorption ranges from 8.94% to 20.05%, exhibiting a difference of 123.98% between the samples, apparent porosity ranges from 17.99% to 36.97%, and a bulk density from 1.844 to 2.013 g/cm³. These values indicate uniform moisture interaction and absence of gel bridging, as expected from the low reactivity of the system at approximately 23 °C.

High porosity indicates poor internal cohesion and open capillary networks, resulting in previously reported low strength (approximately 12 MPa). However, in the case of thermal curing at 80 °C, porosity decreases to 15.93% and 16.46%, and water absorption becomes steady between approximately 7.7% and 7.9%, whereas bulk density was 2.075 g/cm³, approximately 12.5% densification of the lower ambient value of 1.844 g/cm³. This indicates that 80 °C provides enough thermal energy to start the dissolution of $Ca^{2+}$, $Si^{4+}$, and $Al^{3+}$ effectively, resulting in higher uniform N–A–S–H and C–A–S–H gel formation. Under electrical curing at 30 V, the material exhibited an intermediate level of maturity. The average water absorption was approximately 9.1%, ranging between 8.03% and 9.64%. The porosity varied between 16.88% and 19.35%, while the density showed a slight increase, reaching 2.101 g/cm³. The narrow porosity distribution range (within approximately 2.5%) and higher density indicate moderately stable matrix development; though,

the values are still lower compared with the values of higher voltage applications. The Mean Porosity/Density Ratio (PDR) of 0.00894 at 30V is further reduced to approximately 0.0077 for thermal curing, indicating that direct electrical charge at 30V is not enough for standard thermal activation unless energy is constant or increased.

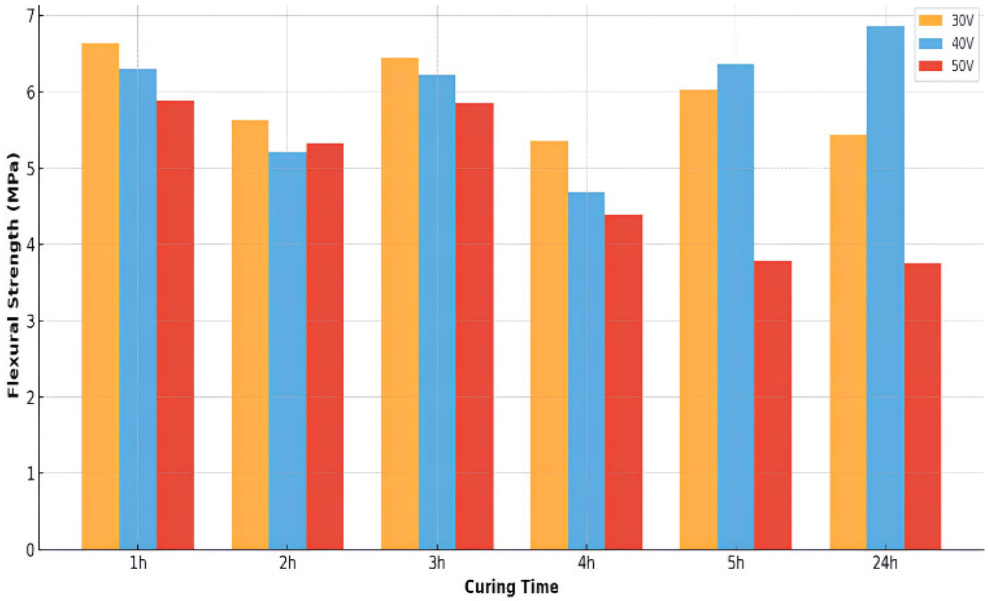


Fig. 6. Comparison of flexural strengths of GCs under 30V, 40V, and 50V electrical curing for 1–24 h.

In comparison, curing under 40V displays the most uniform and best volumetric behavior. Water absorption ranged from 8.07% to 9.37%, with most values tightly clustering between 8.1% and 8.6%, reflecting higher moisture incorporation within the gel network. Porosity varied between 15.98% and 21.11%, whereas bulk densities ranged from 1.984 to 2.344 g/cm³, representing the best packing efficiency among all curing conditions. For example, one of the best specimens (40V in 4 h) had a bulk density of 2.344 g/cm³, corresponding 19.61% porosity, reflecting high compaction and gel continuity. These values were reported for compressive and flexural strengths greater than 25 MPa and 5.5 MPa, respectively. The mean value of PDR at 40V declined to approximately 0.0079, with subsequent values even lower, indicating an efficient internal structuring. These values further reflect that uniform Joule heating is achieved under 40V curing. At the same time, internal temperature stayed near 75–80 °C, with no over-drying of the surface, resulting in deep matrix activation without early shrinkage or cracking.

In the case of 50V curing, lower water absorption (as low as 2.91%) and apparent porosity as low as 6.31%, produce less uniform structural output. The Bulk density under 50V ranged between 2.034 and 2.166 g/cm³. Despite the low porosity and high density, the mechanical strengths after 24 h drop down to approximately 9.7 MPa, a decline of 61% compared to the 40V curing standard. This paradox suggests a critical problem: although a superficially apparent surface densification of 50V is impressive, the process leads to high water evaporation as well as overheating degraded internal phase continuity, yielding a skin-like surface with unreacted as well as cracked interiors. For example, for 50V curing at 4 h, even though the porosity was as low as 6.31%, the density was 2.166 g/cm³. This low strength indicates that the pore structure is neither uniform nor functional. PDR in this case declined to approximately 0.0029. In this case, pore structure appears favorable, but the mechanical collapse indicates that it is structurally empty.

Furthermore, the thermal resistance mismatch caused by overcuring introduces stress concentration zones, further destabilizing the material under load. In short, the results indicate that all curing techniques affect the porosity-density relationships, but 40V electrical curing exclusively harmonizes all volumetric characteristics: it produces bulk densities up to 2.344 g/cm³, intermediate porosity (approximately 16–18%), regulated water absorption (approximately 8.1%), as well as best-in-class gel cohesion, establishing it as the best method for achieving a mature, dense, and resilient geopolymer matrix within 24 h. It is in the threshold voltage where power input (approximately 60 Wh total), resistive heating, ion mobility, as well as microstructural development, converge harmonically, allowing for optimal mechanical and volumetric characteristics, free from the weakening dehydration and the kinetic constraints of subcritical (30V) and supercritical (50V) curing regimes. The analysis confirms that 40V is the optimal electrothermal parameter for inducing ternary GCs under optimized laboratory and mobile field conditions.

The capillary absorption index (I-value), as shown in Figure 7, provides a reliable metric for understanding the transportation properties, reaction maturity, and structural behavior of GCs, especially under electrical curing with 30V, 40V, and 50V, using specimens with constant cross-sectional area. The I-value is defined as the square of the water absorption rate per unit area divided by time and is, therefore, sensitive to both pore connectivity and internal gel network

evolution, making it a reliable indicator of early-stage permeability. At the 60-s mark, the I-value of the 50V series reaches $4.18\times10^{-4}$ g²/cm⁴·s, very high compared to the values of 40V ($1.46\times10^{-4}$) as well as of 30V ($1.09\times10^{-4}$), suggesting that curing under a high voltage of 50V initially leads to much earlier water absorption—almost 286% and 383% higher than for 40V and 30V, respectively. This rapid initial absorption is a consequence of excessive electrothermal stimulation, where there is excessive local Joule heating is caused by a higher voltage, leading to internal matrix temperature elevations above 80 °C within the first hour.

Higher temperature increases the dissolution of aluminosilicate precursors as well as $Na^+$ and $OH^-$ ion mobility. Even though this is favorable to reaction kinetics in some situations, it destabilizes the evolving gel network by inducing expansion stresses. It also leads to the development of microcracks and partial dehydration of the reaction medium. These phenomena create more continuous capillary pathways, allowing rapid water entry. However, the benefit is short-lived; within 1800 s (30 min), the I-value of the 50V series drops by 84.2% to $6.6\times10^{-5}$. This rapid decrease is a sign of premature capillary occlusion, caused by accumulated collapsed gel products and self-healing through microcontraction, clogging water transmission pathways. In contrast, the reduction in I-value for the 40V series is much less severe, only 15.1%, from $1.46\times10^{-4}$ to $1.24\times10^{-4}$. This smaller decrease indicates a more stable, gradually advancing matrix, where capillary pores still exist, allowing water absorption at a uniform, regulated rate. In the case of the 30V series, the lowest I-value of $1.09\times10^{-4}$ decreases by $4.6\times10^{-5}$, a reduction of 57.8%, over the same time, indicating low initial porosity due to under-activated reaction as well as slower, denser pore structure development over time. Although the 30V condition exhibits low permeability, it also demonstrates low strength, indicating insufficient aluminosilicate framework polymerization due to inadequate thermal and ionic stimulation. In contrast, the 50V series benefits from early rapid reaction start-up but is hindered by internal structural discontinuity generated by thermal overshoot and reaction heterogeneity, ultimately affecting mechanical integrity.

TABLE III. WATER ABSORPTION, APPARENT POROSITY, AND BULK DENSITY RESULTS UNDER DIFFERENT CURING REGIMES

| Condition | Dry (wt.) | Sat (wt.) | Immersed (wt.) | Water absorption (%) | Apparent porosity (%) | Bulk density (g/cm³) |
|---|---|---|---|---|---|---|
| Ambient | 234.9 | 255.9 | 139.2 | 8.94 | 17.99 | 2.013 |
| Ambient | 227.9 | 273.6 | 150.0 | 20.05 | 36.97 | 1.844 |
| Thermal | 248.4 | 268.1 | 148.4 | 7.93 | 16.46 | 2.075 |
| Thermal | 248.8 | 267.9 | 148.0 | 7.67 | 15.93 | 2.075 |
| 30V-1h | 272.7 | 298.4 | 163.8 | 9.42 | 19.09 | 2.026 |
| 30V-1h | 253.1 | 277.5 | 151.4 | 9.64 | 19.35 | 2.007 |
| 30V_2h | 252.1 | 275.2 | 150.2 | 9.16 | 18.48 | 2.017 |
| 30V-2h | 257.0 | 280.9 | 153.2 | 9.30 | 18.72 | 2.013 |
| 30V-3h | 250.5 | 273.0 | 149.9 | 8.98 | 18.28 | 2.035 |
| 30V-3h | 243.5 | 266.6 | 146.6 | 9.49 | 19.25 | 2.029 |
| 30V-4h | 244.9 | 266.6 | 146.5 | 8.86 | 18.07 | 2.039 |
| 30V-4h | 262.7 | 286.8 | 156.0 | 9.16 | 18.41 | 2.009 |
| 30V-5h | 260.1 | 281.0 | 157.2 | 8.03 | 16.88 | 2.101 |
| 30V-24h | 239.4 | 260.7 | 143.3 | 8.89 | 18.14 | 2.039 |
| 30V-24h | 283.1 | 308.7 | 168.5 | 9.04 | 18.26 | 2.019 |
| 40V-1h | 297.0 | 322.0 | 172.4 | 8.42 | 16.71 | 1.985 |
| 40V-1h | 289.0 | 314.0 | 168.3 | 8.65 | 17.16 | 1.984 |
| 40V-2h | 256.0 | 280.0 | 150.9 | 9.37 | 18.59 | 1.983 |
| 40V-2h | 259.0 | 283.0 | 169.3 | 9.27 | 21.11 | 2.278 |
| 40V-3h | 268.0 | 289.0 | 157.6 | 7.84 | 15.98 | 2.040 |
| 40V-3h | 266.0 | 288.0 | 155.0 | 8.27 | 16.54 | 2.000 |
| 40V-4h | 296.0 | 320.0 | 174.3 | 8.11 | 16.47 | 2.032 |
| 40V-4h | 263.0 | 285.0 | 172.8 | 8.36 | 19.61 | 2.344 |
| 40V-5h | 268.0 | 290.0 | 158.2 | 8.21 | 16.69 | 2.033 |
| 40V-5h | 287.0 | 313.0 | 169.3 | 9.06 | 18.10 | 1.997 |
| 40V-24h | 260.0 | 281.0 | 153.1 | 8.08 | 16.42 | 2.033 |
| 40V-24h | 270.0 | 292.0 | 158.3 | 8.15 | 16.45 | 2.019 |
| 40V-24h | 270.0 | 292.0 | 158.3 | 8.15 | 16.45 | 2.019 |
| 50V-1h | 282.2 | 297.4 | 161.6 | 5.39 | 11.19 | 2.078 |
| 50V-1h | 252.5 | 266.6 | 144.3 | 5.58 | 11.53 | 2.065 |
| 50V-2h | 276.2 | 288.6 | 156.0 | 4.49 | 9.35 | 2.083 |
| 50V-2h | 291.5 | 305.1 | 164.9 | 4.67 | 9.70 | 2.079 |
| 50V-3h | 261.6 | 276.3 | 147.7 | 5.62 | 11.43 | 2.034 |
| 50V-3h | 277.3 | 292.5 | 158.2 | 5.48 | 11.32 | 2.065 |
| 50V-4h | 287.3 | 300.7 | 162.8 | 4.67 | 9.72 | 2.083 |
| 50V-4h | 257.5 | 265.0 | 146.1 | 2.91 | 6.31 | 2.166 |
| 50V-5h | 271.1 | 284.0 | 152.5 | 4.76 | 9.81 | 2.062 |
| 50V-5h | 264.8 | 276.3 | 149.7 | 4.34 | 9.08 | 2.092 |
| 50V-24h | 255.2 | 266.3 | 143.8 | 4.35 | 9.06 | 2.083 |
| 50V-24h | 246.2 | 257.5 | 138.5 | 4.59 | 9.50 | 2.069 |

To further assess this correlation, a capillary-strength efficiency factor, $\eta_{IC\text{-}S,}$ was calculated as:

$$\eta_{I-CS} = \frac{CS}{I_{1800s}}$$

where CS denotes the compressive strength of the sample. The value of $\eta_{IC\text{-}S}$ was $8.17\times10^{-5}$ for 30V, $3.41\times10^{-5}$ for 40V, and $5.90\times10^{-5}$ for 50V. While 30V yields the highest numerical efficiency, it is deceptive as its low I-value is caused by restricted pore interconnectivity rather than developed well-ordered microstructure. In this case, the achieved strength does not correlate with higher durability or uniform gel development. This is reaffirmed by electrical resistivity ($\rho$), which reflects long-term durability and resistance against ion transportation and shows good agreement with the capillary evaluation results. At 28 days, the electrical resistivity ($\rho$) was the highest for the 30V series (35.2 kΩ·cm), followed by 40V (28.5 kΩ·cm), then the lowest for 50V (21.1 kΩ·cm). This inversely correlates ($R^2 \approx -0.91$) with I-values. The elevated resistivity for 30V is caused by its denser, less reactive matrix, which limits ionic movement. It is a sign of poor binder interface and susceptibility to cracking under load due to a lack of gel bridging. The low resistivity value for 50V indicates its high interconnectivity and retained water, which are commonly characteristic of the loosely developed structure. The 40V series again holds the mid-term balance between both exhibiting sufficient resistivity for long-term stability while still permitting ionic continuity for curing.

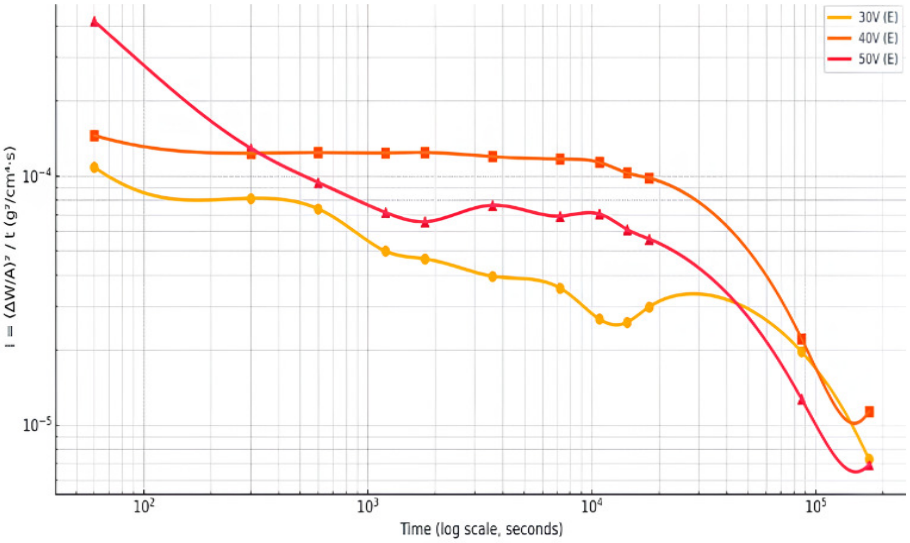


Fig. 7. Capillarity kinetics of electrically-cured GCs as a function of time and voltage.

The calorimetric analysis further provides critical information on the internal reaction kinetics accompanying capillary transport phenomena under different electrical curing regimes. The isothermal calorimetry profiles for all voltage regimes, 30V, 40V, and 50V, display different thermal signatures closely correlated with their respective capillary absorption profiles. In the 50V curing regime, the calorimetric curve is characterized by an early, spiking exothermic peak with a peak heat release rate ($Q_{max} \approx 5.8$ mW/g after around 2 h). The peak value suggests a rapid dissolution of aluminosilicate precursors and the beginning of rapid polycondensation. However, although the initial response indicates high reactivity, the fast, spiking heat evolution also reflects insufficient thermal stability and self-regulation within the system. The rapid energy release is characteristic of runaway geopolymerization bursts that can result in non-uniform gel formation, localized overheating, and internal structural disturbances. This behavior is the precipitous decline of the observed capillary index within the same curing regime.

In contrast, the 30V curing regime displays a much delayed, slower calorimetric response, with $Q_{max} \approx 3.2$ mW/g achieved after around 5.5 h, reflecting a reaction environment that is not able to provide the thermal stimulus necessary for early, efficient dissolution of solid precursors. The extended energy release pattern also correlates with the lower initial I-values and retarded water ingress, indicating a less permeable and less reactive matrix development. The 40V curing regime displays a well-modulated thermal behavior: $Q_{max} \approx 4.6$ mW/g is achieved after around 4 h, reflecting an intermediate between rampant reaction onset and sluggish activation. This moderated, lingering calorimetric peak reflects gradual, but complete geopolymerization with sufficient time for ion diffusion, silicate reorientation, and gel network structuration. Smooth heat flow reflects the steady decrease of the capillary absorption index and indicates a stable, networked pore structure that optimally controls water entry without structural compromise [29-33].

### *C. Microstructural Analysis*

The SEM of the 50S25FA25D changes significantly with the change in curing regime, with each method creating extremely characteristic patterns of gel phase development, precursor conversion, interface cohesion, and general matrix consolidation, as displayed in Figure 8. At ambient conditions, the internal matrix remains underdeveloped with no integrated gel morphology and a prevailing dominance of unreacted primary particles. FA is identifiable as separate spherical bodies, with unaltered and contoured surfaces, with no signs of

surface degradation, dissolution rims, or evidence of a reactive interface. These particles are suspended, unactivated, and within a disconnected binder matrix. This shows that activation energy—thermic or chemical—does not yet exist to undertake significant dissolution or polymer reaction routes. S grains also have a similarly dormant character; angular particles are seen inserted but unmodified, and there are no observable signs of calcium release or gel ring development within the surrounding regions. D grains, with their high-surface-area siliceous form, maintain angular and microporosity, and there is evidence of no gel encapsulation, surface smoothing, or structural degradation.

(a)

(b)

(c)

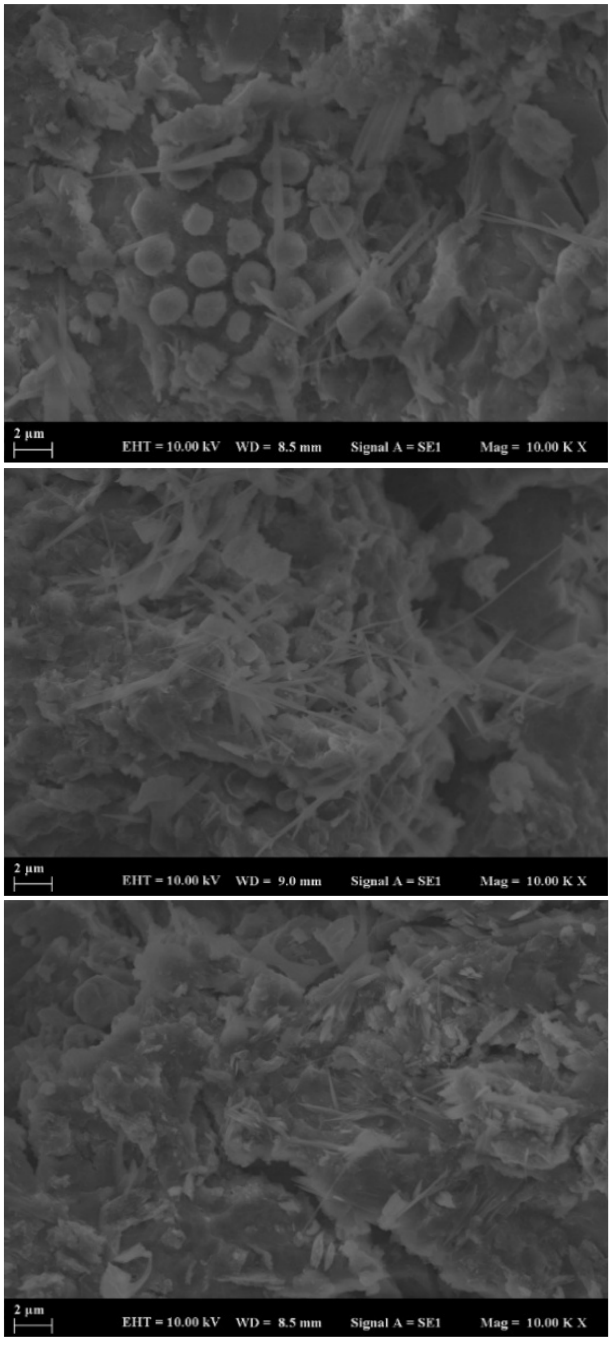


Fig. 8. SEM of 50S25FA25D series: (a) ambient curing, (b) electrical curing, and (c) thermal curing.

The gel phase is patchy and highly discontinuous, occurring as separate patches with irregular boundary lines and minimal interlinkage within the reaction domains. Binder network possesses many capillary voids, loosely retained phase boundary regions, and microcracks that often occur along the particle–binder transition areas. This behavior indicates internal desiccation stress and a brittle network with no polymer-based resiliency. The absence of a progressive gradient within the micrographs signals a lack of volumetric homogeneity, and the binder fails to form effective bridging across aggregates, leaving the matrix in a chemically disjointed and mechanically weak condition.

Under 40V electric curing, the mortar experiences extreme microstructurally transformed properties, although improvement is still spatially uneven and a function of distance from current flow paths. The FA phase engages with the geopolymerization reaction, with many particles showing softened outlines, pitted surfaces, and broken contours. These features suggest partial depolymerization and leaching of silica and alumina. Reaction rims appear on some spheres, signaling early dissolution and partial anchoring of the gel, although full integration into the matrix is not always accomplished uniformly. S grains undergo more extensive ion exchange, creating perceptible C–A–S–H gel regions surrounding and connecting contiguous phases. However, the regions are of variable thickness and distribution. Some particles of D exhibit dual character—some areas contain grains showing early coating with gel and blurred textural contours. At the same time, other parts maintain their initial morphology, implying uneven thermal and ionic accessibility. Vitrified surface areas near electrode boundaries indicate that extreme localized heat produces rapid solidification, phase densification, and possible surface sealing, hindering inward gel propagation and creating microstructurally asynchrony. These thermally concentrated regions contain microvoids and stress fissures that extend radially or longitudinally, further breaking up the gel matrix.

Gel connectivity was observed in several linked regions, forming amorphous bridges and early networked domains, but large areas maintain poor integration of phases and lack a complete, structurally evolved form. The textural contrast within the field indicates extreme densification gradients, and binder porosity remains variable. Electrical curing, thus, delivers extensive early energy input with the capability to activate the S and partially react with the FA and D phases. Still, thermal gradient and rapid-setting dynamics produce heterogeneity and limit complete matrix homogeneity unless power distribution is optimized. Thermal curing at 80 °C for 24 h produces the most structurally cohesive and chemically evolved matrix, resulting in a homogeneous amorphous binder phase with minimal porosity and maximum phase interaction. No spherical residue of FA remains, with all FA particles being completely decomposed, absorbed into a continuous gel network, and undistinguishable from the surrounding mass. S grains have degraded surfaces, immersed within a dense, homogeneous gel matrix where expansive C–A–S–H zones bind tightly with surrounding domains. Amorphous matrix fills former void spaces without indicating phase separation, shrinkage cracking, or delamination. D evolves from a distinct angular phase to a diffuse siliceous contribution within the

amorphous network, no longer preserving its original porous texture but instead blending smoothly with corresponding alkaline-activated silicate and alumina-bearing phases to produce integrated N–A–S–H contributions. The matrix has continuous connectivity on all scales, with no indication of rapid textural changes or localized failure surfaces. Gel is smooth and isotropic, blending nodular and fibrous morphologies, and filling interfacial spaces with no discernible boundary weakness. Surface texture is uniform throughout the microscope's view, and no areas of uncontrolled heat propagation or regions of vitrification break up the morphology. Dense ITZ-similar zones occur at the binder–aggregate interface, removing mechanical discontinuity. At high magnification, the gel mass has a homogenous contrast, a sign of effective ion transport, sustained gelation, and a fully mature three-dimensional polymer network. All previously distinct phases are completely assimilated into a homogeneous geopolymeric system.

The XRD of the 50S25FA25D is largely amorphous with a broad hump that stretches from around 25° to 35° 2θ, which is a clear indication of an aluminosilicate gel network. This diffuse band is consistent with the disordered polymeric phases commonly prevalent under geopolymerization, with sodium and calcium-based aluminosilicate hydrates (N–A–S–H and C–A–S–H gels). The diffuse pattern is a marker for the occurrence of extensive precursor dissolution and subsequent gel development. The occurrence of the amorphous halo indicates that FA and D were actively engaged in geopolymer matrix development and made substantial contributions toward the development of a polymerized, three-dimensional network. Several superposition crystalline reflections occur on this background, albeit with relatively weak intensity. This signifies that the geopolymerization reaction had proceeded to a high reaction extent, but with no complete response of all crystalline precursors present. Specifically, at around 26.6° and 27.9° 2θ, distinct reflections correspond to quartz and mullite, respectively; both are thermally and chemically robust phases usually retained from raw FA and D sources. These residual crystalline peaks are markers for the partial susceptibility of the aluminosilicate components, particularly those with a dense structural form less aggressive toward alkaline attack, e.g., mullite, which resists depolymerization under usual activation regimes.

Besides those main crystalline phases, there are weaker reflections at about 36.5°, 50.1°, and 59.9° 2θ, possibly due to calcium-magnesium silicate species, e.g., gehlenite or akermanite, which exist as unreacted residues from the S component or as secondary crystallization products after partial reaction, as displayed in Figure 9. The appearance of those phases indicates that although S assisted well toward the production of calcium-rich gel, not all crystalline areas within it were dissolved into the amorphous matrix. Significantly, the XRD fails to disclose any prominent peaks corresponding to portlandite ($Ca(OH)_2$) or calcite ($CaCO_3$) since calcium ions available during the activation of the S were effectively immobilized within the gel without precipitating as crystallized hydroxides or carbonates.

(a)

(b)

(c)

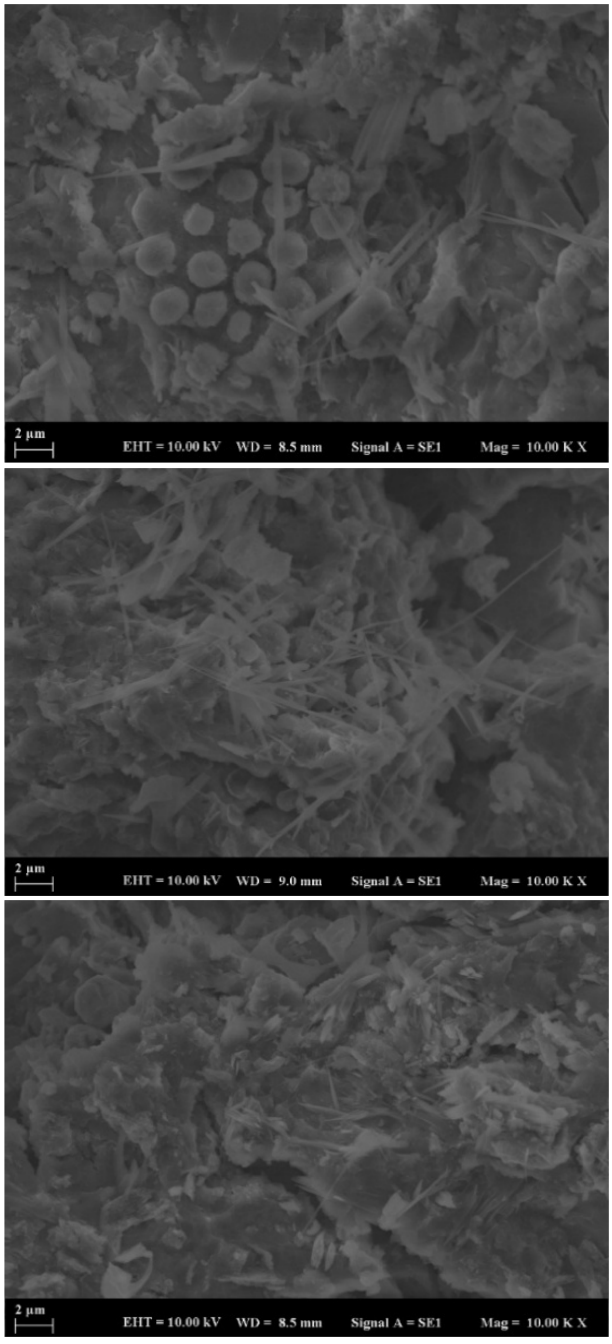


Fig. 9. SEM of 50S25FA25D series: (a) ambient curing; (b) electrical curing; (c) thermal curing.

The superposition is further evidence for the compelling character of the alkaline activation process and the chemical stability of the resulting binder matrix. The total peak intensity on the diffractogram remains moderate, and the dominance of the amorphous envelope over crystalline signals indicates a well-developed but diverse matrix, where most of the reacting phases participated in gelation, but a small fraction remained stably conserved. The coexistence of a broad amorphous envelope and weak crystalline signals is a sign of the ternary interaction of components of the FA, D, and S within the current system, with each being variably reactive under the

same mixing and curing regime. This diffraction response validates the microstructure complexity of the blend 50S25FA25D. It is consistent with SEM-based interpretations, where partial development of gelation, residual phase distribution, and inter-particle consolidation varied from domain to domain, forming a very polymerization-efficient geopolymer matrix but with locally un-reacted or semi-reactive precursor phases conserved.

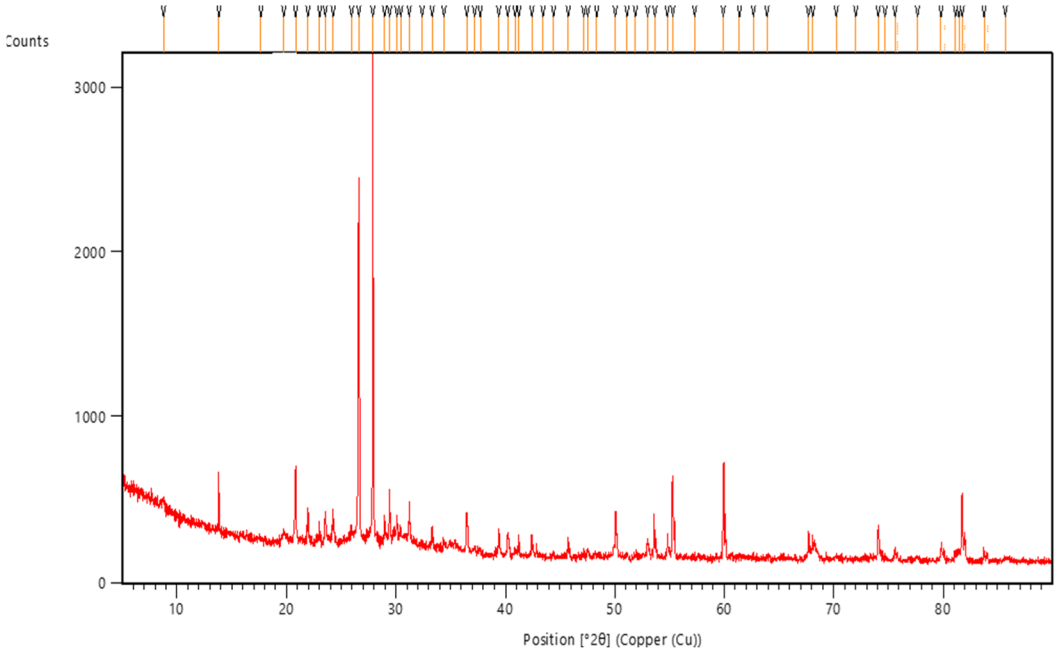


Fig. 10. XRD of 50S25FA25D series.

TABLE IV. SUMMARY OF EXPERIMENTAL VARIABLES AND THEIR OBSERVED EFFECTS ON PERFORMANCE PARAMETERS

| Variable category | Variable / Level | Impact on results |
|---|---|---|
| Mix composition | 1000P, 100D | Observed to possess the weakest mechanical strength (<6.5 MPa) after thermal curing due to the limited chemical activity. Mostly used in the form of inert filler material, having experienced poor microstructural gel formation coupled with partial matrix densification. |
| Mix composition | 50S25D25FA | Attained the highest compressive strength (maximum 31.72 MPa) and flexural strength (6.88 MPa) through 40V electrical curing. Mutual interaction of S (supply of Ca2+), FA (aluminosilicate source), and D (amorphous SiO2 and buffering of porosity) contributed to good gel continuity and low porosity. |
| Mix composition | 50S25OP25FA | Moderate gain in strength (20 MPa thermally cured), limited long-term gain due to OP's inert properties. OP enhanced packing but disrupted gel connectivity, and failed to contribute substantially to polymerization or strength preservation. |
| AB Ratio | 0.7 | Identified as the optimal ratio, consistently yielding the highest compressive and flexural strengths across curing methods. Enabled adequate alkali activation while preventing excessive free water that could lead to microcracking or porosity. |
| AB Ratio | 1.1–1.4 | Led to over-saturation of activators, poor workability, and inconsistent setting. Associated with increased internal porosity and lower strength due to gel destabilization and water retention issues. |
| Curing regime | Ambient | Inadequate geopolymerization at approximately 23 °C; compressive strengths were less than 14 MPa. SEM analysis detected poor matrix continuity, unreacted particles, and insignificant gel phase formation. |
| Curing regime | Thermal (80°C, 24h) | Substantially increased dissolution and condensation of reactive species; improved mechanical strength, porosity, and gel formation. A homogeneous amorphous gel matrix was observed in the SEM in fully integrated precursors. |
| Curing regime | Electrical (30V, 40V, 50V) | Optimal curing was 40 V: internal matrix temperature attained approximately 76–90 °C to produce high early strength, excellent gel morphology, and optimal energy efficiency (0.344 MPa/W.h). At 30 V, the samples were undercured, while 50 V they were overheated and microcracked internally. |
| Curing duration | 1h–24h | Compressive strength plateaued immediately after 3-5 h at 40V; longer curing improved the flexural resistance and porosity control. The 40V-4h had the best balance for mechanical and workability performance. |
| Mechanical properties | Compressive, flexural strength | The 50S25D25FA under 40V–4h: 31.72 MPa compressive, 6.88 MPa flexural. Lowest strength: ~1.8 MPa in 100D matrix. High-performance systems exhibited high strength-to-porosity synergy factors. |
| Physical properties | Water absorption, porosity, bulk density | Lowest porosity (15.96–16.47%) and water absorption (<8.1%) at 40V–4h. The 50V gave a superficially denser microstructure but a structurally unstable interior. The 30V yielded denser but underdeveloped matrices. |
| Microstructure | SEM, XRD | Thermal curing offered complete gel continuity along with the lack of phase segregation. The 40V generated well-developed polymeric gel networks. Ambient curing offered disconnected particles, poor gel coverage, and unreacted regions. |

## IV. CONCLUSIONS

This study presents a novel constitution of ternary Geopolymer Composites (GCs) consisting of Kazakhstan-sourced Slag (S), Fly Ash (FA), Diatomite (D), and Opacifier waste (OP). The findings demonstrated that electrothermal curing at 40 V AC outperforms conventional thermal curing. Electrothermal curing resulted in higher mechanical strength, energy saving, and matrix integrity with significantly reduced energy input. Due to its unusually high amorphous silica percentage and native porosity, D acted as an ultra-reactive secondary precursor to foster broad-based gel nucleation, and achieved 31.72 MPa compressive and 6.06 MPa flexural strength under 80 °C heat curing. In contrast, the utilization of the largely inertacting OP functioned as a filler, achieving just 19.80 MPa compressive and 4.01 MPa flexural strength. This highlights the role of chemical reactivity in strength development. The curing regime and method of activation had a significant influence: the ambient curing environment resulted in a compressive strength of 13 MPa, while the typical heat curing enhanced performance by ~129% and reduced porosity by ~12%, confirming thermally driven aluminosilicate dissolution and gel formation. The most important finding of the current study lies in 40V electrothermal curing, which achieved a maximum compressive strength and flexural strength of 30.63 MPa and 6.88 MPa, respectively. With an electrical energy consumption of approximately 60 Wh, electrothermal curing achieved about 60% higher strength compared to other curing regimes.

These results are in good agreement with the finding of [29], which compared direct electrical curing and traditional steam curing of hydraulic cement-based materials within the same sets of thermal regimes (40 °C, 60 °C, 80 °C). The study demonstrated that electrical curing and traditional steam curing in their initial phases improved hydration. However, electrical curing-treated mortars consistently had finer pore structures, superior transition-to-gel ratios, and elevated early compressive strength. Electrical curing specimens in particular achieved superior microstructural compactness and mechanical strength while consuming up to 8.6 times less energy than the specimens of the steam curing method, therefore validating the inherent volumetric and self-controlling heat advantages of Joule-driven curing. In the 80 °C curing, there were similar gains in compressive strength for electrical curing and steam curing specimens, but electrical curing achieved the same through a much narrower energy footprint of 1.03 kW compared to 2.35 kW/batch for steam curing. This establishes electrical curing as a low-carbon and efficient method.

The capillary performance also improved with only 15.1% capillary absorption index (I-value) under 40V curing, confirming robust pore closure and continued matrix densification. Deviations from the optimum voltage had significant negative consequences. Under-curing with 30V led to defective matrices of only 15.76 MPa, while 50 V over-curing resulted in internal overheating and micro-fragments, reducing compressive strength to 9.7 MPa from 19.74 MPa, about 50.8% decline in compressive strength.

The SEM and XRD results revealed that curing under 40V and 80 °C resulted in near-full dissolution of S and FA, producing dense N-A-S-H and C-A-S-H colloidal particles, whereas curing in ambient conditions conserved heterogeneous, porous matrices of unreacted particles. The findings of the present study either match or outperform current literature benchmarks while consuming less energy and using simpler processes. Authors in [23] also demonstrated how the replacement of FA or metakaolin by the D in 1–3 wt% under 75 °C curing led to a reduction in compressive strength of up to 28%. The strength reduced from 45 MPa (reference) to 32.4 MPa ± 3 MPa for FA3AD after 28 days. In contrast, the strength replacement of 5 wt% of sand by the D increased the strength of the binder paste by ~24%, up to 47 MPa. Authors in [20] achieved 42.4 MPa with only 3% D under 60 °C in 72 h, whereas the proposed system attained 30.63 MPa with 25% D under 3 h of 40V curing.

Authors in [34] presented an in-depth literature review of 20+ experimental studies and concluded that the DE-blended geopolymer systems, activated by the common alkali solutions (e.g., $NaOH/Na_2SiO_3$), generally obtained 5.78 MPa–106 MPa compressive strength, of which 15–30% of the weight replacement of the raw material by the calcined form generated the optimum mechanical results. For example, 15% of calcined D addition to the high-calcium FA produced 64 MPa of compressive strength in 60 °C heat curing, while the raw-DE-based systems often needed to be sintered in the range of 850–1100 °C or even to the level of the autoclave treatment to reach a moderate strength of 8–28 MPa. Nevertheless, the proposed system yielded 30.63 MPa in 3 h of 40V electrothermal curing without the use of high-temperature sintering and long-lasting heat exposure. Moreover, the proposed system reduced curing time by ~96% and temperature by ~25–45 °C compared to the common D-based systems.

Finally, the literature review revealed the lack of true clinker-free, fiber-reinforced, and digitally controlled curing methods focusing on D-based geopolymer. However, the findings of the present study not only emphasize the strength-energy ratio but also propose a quick, scalable, and low-energy-consumption method for raw material activation. Even the high-strength ferrochrome-slag systems developed in [35], reaching 50 MPa at 100 °C, fail to address the sustainability aspect. No prior study comprehensively integrates early-age strength (20.76 MPa at 3 h, retained to 24 h), porosity reduction (~12%), capillary control, and mechanical-energy measurements in a single system using S-FA-D mixtures.

This study presents proof of concept for off-the-shelf material-based high-performance electrothermal curing alongside the introduction and application of new metrics such as Strength Retention Ratio (SRR), Flexural Strength Thermal Enhancement Ratio (FSTER), and capillary-strength efficiency factor ($\eta_{IC\text{-}S}$). These metrics can be utilized to characterize the electrical curing's complex performance behavior. When used in conjunction with validation through SEM/XRD, these metrics allow for the tight control of geopolymer kinetics. These metrics can also be used for the development of geopolymer technology for application in cold climates, remote, and low-infrastructure sites.

The findings of this study also provide future directions for the development of adaptive curing regimes with

algorithmically controlled voltage, duration, and mix design through smart power grid and/or AC photovoltaic inverter feedback, further enhancing the sustainability of the energy system. Overall, the study outlines an optimized geopolymer design outperforming conventional heat-curing methods, while also advancing material science through the application of a measurable, energy-efficient curing regime, aligned with the circular economy.

## DATA AVAILABILITY STATEMENT

The data supporting the findings of this study are available from the corresponding author upon reasonable request.

## REFERENCES


[1] B. Coppola, J.-M. Tulliani, P. Antonaci, and P. Palmero, "Role of Natural Stone Wastes and Minerals in the Alkali Activation Process: A Review," *Materials*, vol. 13, no. 10, May 2020, Art. no. 2284, https://doi.org/10.3390/ma13102284.

[2] A. Tukaziban, C.-S. Shon, G. Kareken, N. Kozhageldi, D. Zhang, and J. R. Kim, "Evaluation of Properties of Energy-Efficient Geopolymer Cellular Concrete Containing Basic Oxygen Furnace Slag Aggregate," *Materials Today: Proceedings*, Oct. 2023, Art. no. S2214785323049994, https://doi.org/10.1016/j.matpr.2023.10.094.

[3] G. Z. Alzhanova *et al.*, "Development of Environmentally Clean Construction Materials Using Industrial Waste," *Materials*, vol. 15, no. 16, Aug. 2022, Art. no. 5726, https://doi.org/10.3390/ma15165726.

[4] K. Aryngazin and A. Abisheva, "Use of Recycled Waste in the Production of Building Materials," *Technobius*, vol. 2, no. 2, June 2022, Art. no. 0020, https://doi.org/10.54355/tbus/2.2.2022.0020.

[5] L. Y. Ming, O. W. En, H. C. Yong, M. M. A. B. Abdullah, and O. S. Ween, "Characteristic of One-Part Geopolymer as Building Materials," in *Sustainable Waste Utilization in Bricks, Concrete, and Cementitious Materials*, vol. 129, A. Abdul Kadir, N. Amira Sarani, and S. Shahidan, Eds. Singapore: Springer Singapore, 2021, pp. 97–118.

[6] T. Luukkonen, Z. Abdollahnejad, J. Yliniemi, P. Kinnunen, and M. Illikainen, "One-Part Alkali-Activated Materials: A Review," *Cement and Concrete Research*, vol. 103, pp. 21–34, Jan. 2018, https://doi.org/10.1016/j.cemconres.2017.10.001.

[7] T. Mukhametkaliyev, Md. H. Ali, V. Kutugin, O. Savinova, and V. Vereschagin, "Influence of Mixing Order on the Synthesis of Geopolymer Concrete," *Polymers*, vol. 14, no. 21, Nov. 2022, Art. no. 4777, https://doi.org/10.3390/polym14214777.

[8] P. Chindaprasirt and U. Rattanasak, "Calcium Wastes as an Additive for a Low Calcium Fly Ash Geopolymer," *Scientific Reports*, vol. 13, no. 1, Sept. 2023, Art. no. 16351, https://doi.org/10.1038/s41598-023-43586-w.

[9] G. Zhakypova, S. Uderbayev, N. Saktaganova, G. Abyieva, A. Budikova, and A. Zhapakhova, "Properties of Fine-Grained Concrete Using Ash of Kazakhstan," *Evergreen*, vol. 10, no. 2, pp. 830–841, June 2023, https://doi.org/10.5109/6792835.

[10] S. Qaidi *et al.*, "Fly Ash-Based Geopolymer Composites: A Review of the Compressive Strength and Microstructure Analysis," *Materials*, vol. 15, no. 20, Oct. 2022, Art. no. 7098, https://doi.org/10.3390/ma15207098.

[11] M. Statkauskas, D. Vaičiukynienė, and A. Grinys, "Mechanical Properties of Low Calcium Alkali Activated Binder System Under Ambient Curing Conditions," *Scientific Reports*, vol. 14, no. 1, June 2024, Art. no. 13060, https://doi.org/10.1038/s41598-024-63808-z.

[12] M. Nurpeisova, Z. Estemesov, S. Gabbasov, A. Ashimova, and A. Bek, "Studying the Properties of Ash and Slag Waste for Use in the Manufacture of Construction Products," *Mining of Mineral Deposits*, vol. 17, no. 3, pp. 102–109, Sept. 2023, https://doi.org/10.33271/mining17.03.102.

[13] M. Lei, X. Wang, H. Meng, Z. Yan, J. Lin, and Z. Wu, "Study of Fly Ash-Slag Geopolymer Mortar as a Rapid Strengthening Agent for Concrete Structures," *Construction and Building Materials*, vol. 394, Aug. 2023, Art. no. 132147, https://doi.org/10.1016/j.conbuildmat.2023.132147.

[14] H. S. Abhishek, S. Prashant, M. V. Kamath, and M. Kumar, "Fresh Mechanical and Durability Properties of Alkali-Activated Fly Ash-Slag Concrete: A Review," *Innovative Infrastructure Solutions*, vol. 7, no. 1, Feb. 2022, Art. no. 116, https://doi.org/10.1007/s41062-021-00711-w.

[15] Y. Lv, C. Wang, W. Han, X. Li, and H. Peng, "Study of the Mechanical Properties and Microstructure of Alkali-Activated Fly Ash–Slag Composite Cementitious Materials," *Polymers*, vol. 15, no. 8, Apr. 2023, Art. no. 1903, https://doi.org/10.3390/polym15081903.

[16] K. Şahbudak, "Mechanical and Thermal Evaluation of Diatomite Doped Fly Ash Based Geopolymers," *Materials Science*, vol. 28, no. 1, pp. 75–81, Feb. 2022, https://doi.org/10.5755/j02.ms.26796.

[17] C. Bagci, G. P. Kutyla, and W. M. Kriven, "Fully Reacted High Strength Geopolymer Made with Diatomite as a Fumed Silica Alternative," *Ceramics International*, vol. 43, no. 17, pp. 14784–14790, Dec. 2017, https://doi.org/10.1016/j.ceramint.2017.07.222.

[18] H. Mohamedbakr and M. Burkitbaev, "Elaboration and Characterization of Natural Diatomite in Aktyubinsk/Kazakhstan," *The Open Mineralogy Journal*, vol. 3, no. 1, pp. 12–16, June 2009, https://doi.org/10.2174/1874456700903010012.

[19] K. Pławecka, A. Bąk, M. Hebdowska-Krupa, and M. Łach, "The Use of Calcined Diatomite as an Additive to Geopolymeric Materials," in *10th MATBUD 2023 Scientific-Technical Conference*, Feb. 2023, Art. no. 28, https://doi.org/10.3390/materproc2023013028.

[20] S. Ilkentapar and E. Orklemez, "Uçucu Kül Esaslı Geopolimer Harçlara Diatomit İkamesinin Isı İletkenliğe Etkisi," *Erciyes Üniversitesi Fen Bilimleri Enstitüsü Dergisi*, vol. 36, no. 3, pp. 312–324, 2020.

[21] X. Ge, X. Hu, H. Li, and C. Shi, "Synergistic Effect of Characteristics of Raw Materials on Controlling the Mechanical Properties of Fly Ash-Based Geopolymers," *Cement and Concrete Composites*, vol. 145, Jan. 2024, Art. no. 105368, https://doi.org/10.1016/j.cemconcomp.2023.105368.

[22] X. Guan, W. Luo, S. Liu, A. G. Hernandez, H. Do, and B. Li, "Ultra-High Early Strength Fly Ash-Based Geopolymer Paste Cured by Microwave Radiation," *Developments in the Built Environment*, vol. 14, Apr. 2023, Art. no. 100139, https://doi.org/10.1016/j.dibe.2023.100139.

[23] M. Nykiel *et al.*, "The Influence of Diatomite Addition on the Properties of Geopolymers Based on Fly Ash and Metakaolin," *Materials*, vol. 17, no. 10, May 2024, Art. no. 2399, https://doi.org/10.3390/ma17102399.

[24] T. Nongnuang, P. Jitsangiam, U. Rattanasak, and P. Chindaprasirt, "Novel Electromagnetic Induction Heat Curing Process of Fly Ash Geopolymer Using Waste Iron Powder as a Conductive Material," *Scientific Reports*, vol. 12, no. 1, June 2022, Art. no. 9530, https://doi.org/10.1038/s41598-022-13392-x.

[25] Y. Zhang *et al.*, "Electrothermal Effect of Alternating Current on Hardening Process of Metakaolin-Based Geopolymer," *Cement and Concrete Composites*, vol. 142, Sept. 2023, Art. no. 105205, https://doi.org/10.1016/j.cemconcomp.2023.105205.

[26] S. Vaidya, E. I. Diaz, and E. N. Allouche, "Experimental Evaluation of Self-Cure Geopolymer Concrete for Mass Pour Applications," in *World of Coal Ash (WOCA) Conference*, Denver, CO, USA, May 2011.

[27] S. Abubakri, P. S. Mangat, V. Starinieri, and G. R. Lomboy, "Electric Curing Parameters of Mortar and its Mechanical Properties in Cold Weather," *Construction and Building Materials*, vol. 314, Jan. 2022, Art. no. 125615, https://doi.org/10.1016/j.conbuildmat.2021.125615.

[28] J. Cai, X. Li, J. Tan, and B. Vandevyvere, "Fly Ash-Based Geopolymer with Self-Heating Capacity for Accelerated Curing," *Journal of Cleaner Production*, vol. 261, July 2020, Art. no. 121119, https://doi.org/10.1016/j.jclepro.2020.121119.

[29] Z. Yang *et al.*, "A Comparative Study on the Mechanical Properties and Microstructure of Cement-Based Materials by Direct Electric Curing and Steam Curing," *Materials*, vol. 14, no. 23, Dec. 2021, Art. no. 7407, https://doi.org/10.3390/ma14237407.

[30] A. Yvette Sunga, S. Abubakri, G. Lomboy, I. Mantawy, D. Kennedy, and B. Watts, "Electric Curing of Conductive Concrete for Cold Weather," presented at the IABSE Symposium, Manchester 2024: Construction's Role for a World in Emergency, Manchester, United

Kingdom, 2024, pp. 789–797, https://doi.org/10.2749/manchester.2024.0789.

[31] M. I. Batyuk, A. I. Gnyrya, V. Y. Ushakov, and S. V. Korobkov, "Rapid Direct Electric Heating of Fresh Concrete," *Journal of Physics: Conference Series*, vol. 1989, no. 1, Aug. 2021, Art. no. 012024, https://doi.org/10.1088/1742-6596/1989/1/012024.

[32] T. Uygunoğlu and İ. Hocaoğlu, "Effect of Electrical Curing Application on Setting Time of Concrete with Different Stress Intensity," *Construction and Building Materials*, vol. 162, pp. 298–305, Feb. 2018, https://doi.org/10.1016/j.conbuildmat.2017.12.036.

[33] M. S. Amouri and N. M. Fawzi, "The Mechanical Properties of Fly Ash and Slag Geopolymer Mortar with Micro Steel Fibers," *Engineering, Technology & Applied Science Research*, vol. 12, no. 2, pp. 8463–8466, Apr. 2022, https://doi.org/10.48084/etasr.4855.

[34] J. J. Kipsanai, P. M. Wambua, S. S. Namango, and S. Amziane, "A Review on the Incorporation of Diatomaceous Earth as a Geopolymer-Based Concrete Building Resource," *Materials*, vol. 15, no. 20, Oct. 2022, Art. no. 7130, https://doi.org/10.3390/ma15207130.

[35] Ş. Koçyiğit, "Performance Evaluation of Geopolymer Mortars Containing Waste Ferrochrome Slag and Fly Ash for Sustainable Green Building," *Scientific Reports*, vol. 14, no. 1, June 2024, Art. no. 14606, https://doi.org/10.1038/s41598-024-65552-w.